Title
Spatial Frustration: Using Pharmacological and Mechanical Disruption of Membrane Receptor Transport to Probe Cell Signaling Dynamics on Supported Lipid Bilayers

Author
Petit, Rebecca

Publication Date
2013

Peer reviewed|Thesis/dissertation

Spatial Frustration: Using Pharmacological and Mechanical Disruption of Membrane Receptor Transport to Probe Cell Signaling Dynamics on Supported Lipid Bilayers

By

Rebecca Suzanne Petit

A dissertation submitted in partial satisfaction of the

requirements for the degree of

Doctor of Philosophy

in

Chemistry

in the

Graduate Division

of the

University of California, Berkeley College of Chemistry

Committee in charge:

Professor Jay Groves, Chair
Professor John Kuriyan
Professor Jeremey Thorner

Abstract

Spatial Frustration: Using Pharmacological and Mechanical Disruption of Membrane Receptor Transport to Probe Cell Signaling Dynamics on Supported Lipid Bilayers

by

Rebecca Suzanne Petit

Doctor of Philosophy in Chemistry

University of California, Berkeley

Professor John T. Groves, Chair

Micron-scale spatial reorganization of cell membrane receptor protein clusters is emerging as an important early modulator of inter- and intracellular signaling input. Detailed within is an in-vitro investigative technique utilizing cultured cells, nanolithograpically-patterned supports for fluid biomolecule-functionalized phospholipid bilayer membranes and inverted optical microscopy. This method allows the user to visualize and, if desired, restrict the formation and transport of these transient macroclusters as they coalesce on the membrane of a stimulated cell. Multi-color fluorescence imaging allows the simultaneous tracking of multiple molecules, permitting real-time analysis of coupling between surface receptors and intracellular signaling and structural proteins. The two systems examined are the T cell immunological synapse and ephrinA1-EphA2 interactions in highly invasive breast cancer cells. In both cases, it is demonstrated that induced restrictions of receptor-mediated cytoskeletal reorganization is sufficient to alter downstream signaling outcomes, and the molecular mechanisms of feedback coupling are investigated.

Table of Contents

Introduction: The Supported Lipid Bilayer Platform

Silica-supported lipid bilayer membranes figure prominently in all investigations detailed in this dissertation. This unique platform recapitulates the laterally fluid context in which these systems natively function. By virtue of residing in a two-dimensional fluid, membrane receptors exhibit extraordinary sensitivity to physical characteristics of their environment that are not present in the context of soluble proteins, such as spatial organization[1], polyvalency[2], and mechanical strain[3]. An understanding of any of these effects on cell signaling requires a platform that accurately reflects the physiological context in which these proteins are presented. The elucidation of molecular mechanisms in cell biology typically requires the use of analytic methods in which cell receptor reorganization is perturbed and the effect of the disturbance on downstream signaling events is characterized. In this work, two such perturbational methods are utilized. The first, that of biochemical inhibition that targets specific components of the cytoskeletal membrane receptor transport machinery, allows the researcher to attribute changes in downstream signaling effects to specific elements of known signaling pathways, while the second, that of patterning lateral diffusion barriers onto the lipid bilayer substrate, allows the researcher to determine the effects of mechanical force and receptor/ligand cluster repartitioning on the response of the cell.

Here, we describe methods to introduce spatial constraints on the organization of membrane receptors, thus aiding in the elucidation of the physical mechanisms that are unique to cell surface signaling pathways. We begin with a brief description of the chemical properties of phospholipids that allow them to self-assemble into two-dimensionally fluid arrays.

Phospholipids

Phospholipids[4] (**Figure 1, top**) are the primary components of lipid membranes. They are composed of a polar "head" on one end and a nonpolar "tail" on the other. The polar head group consists of one of several small organic molecules (**Figure 1, bottom**), and a phosphate group to carbon 3 of a glycerol moiety. Carbons 1 and 2 of this moiety are each linked via carboxyl ester to a fatty acid (See **Tables 1 and 2** for common examples), the aliphatic chains of which constitute the hydrophobic tail groups. Due to their amphipathic character, phospholipids are soluble in both aqueous and organic liquids, and tend to self-assemble into monolayers at interfaces between two mediums that differ significantly in hydrophilicity. When present in aqueous media above a critical concentration, phospholipids can aggregate to form various types of supramolecular structures, the formation of each being more or less favorable depending on parameters such as the head group size and charge, tail group length and shape, solution temperature and ionic strength, and the presence of multiple types of phospholipids or additional surfactant molecules. Excepting micelles, these structures have surfaces composed of a bilayer membrane, which consists of two lipid monolayer leaflets arranged with the

hydrophobic tail chains of the two layers facing towards one another and the heads facing outward towards solution. Such a configuration minimizes phospholipid-solution interface tension by allowing polar interactions between water molecules and lipid head groups while excluding water from the nonpolar aliphatic tail chains of the membrane's core.

A key characteristic of phospholipid bilayer membranes is their phase behavior. A phospholipid molecule is held in the plane of the bilayer mainly by attractive Van der Waals forces between its hydrophobic tail groups and those of neighboring molecules. At low temperatures, these forces lock the tail groups into a crystalline solid phase. At higher temperatures, the alkyl groups in the tails gain the ability to rotate freely, enabling them to change places with one another and thus experience random lateral diffusion over the surface of the bilayer. T_m, the temperature at which the bilayer experiences this phase change, decreases with increasing chain length (which adds to the magnitude of inter-lipid Van der Waals attractive force) and saturation of the fatty acid tail groups (which minimizes lipid packing energy).

Supported Lipid Bilayers

Like cellular plasma membranes present in cells, supported lipid bilayers are composed of two lipid monolayer leaflets arranged with the hydrophobic tail sides of the two layers in close contact with one another. In a cell's plasma membrane, the hydrophilic head groups of the inner leaflet face the cytoplasm, and those of the outer leaflet face the extracellular fluid. In the SLB, the upper leaflet's head groups face into an aqueous solution, while the lower leaflet's head groups face a solid hydrophilic support, usually silica or mica, with a thin (~1nm) layer of hydration sandwiched between the support and the lower leaflet[5]. The forces sustaining the bilayer's association with the substrate hang in a delicate balance: they must be great enough to prevent detachment, but not so great that lipids adsorb to the surface and become immobile. The hydration layer serves to prevent the latter fate. Strongly stabilized by hydrogen bonding and charge-dipole interactions with the substrate and lipid head groups, this layer establishes a spatial separation between the two surfaces and facilitates lateral head group diffusion across the substrate plane. Through judicious selection of the combination of lipids used to form the bilayer, the researcher can create membranes exhibiting the desired degree of fluidity.

Another useful feature of phospholipids is that their head groups can be functionalized with linker moieties through which biologically relevant molecules can be attached to the bilayer[6,7]. Some of these linkage schemes include biotin-streptavidin affinity binding[8], polyhistidine-Ni^{2+} coordination chemistry[9] or direct covalent coupling using thiol-reactive groups targeting cysteine residues[10]. For greater ligand diversity, orthogonal chemical linkage schemes may be even combined on the same bilayer. The density of the desired ligands can be easily controlled merely by adjustment of the ratios of linker-functionalized lipids to those without linker. To aid in bilayer fluidity characterization, fluorophore may also be chemically coupled to lipids for convenient imaging via immersion or inverted fluorescence microscopy.

Cells deposited onto the bilayer are able to interact with the biomolecules attached to the bilayer via relevant surface receptor proteins. If the bilayer is functionalized with fluorophore-labeled proteins, the rearrangements resulting from cell actions on the bilayer can be easily imaged using epifluorescence microscopy. Total internal reflection microscopy (TIRF) proves useful when imaging cell immunostains or transfected fluorescent proteins, and confocal microscopy can be used to construct z-stacks of a cell. Areas of close contact between the cell and the underlying substrate can be easily discerned with refraction interference contrast microscopy (RICM).

Patterning Supported Membranes

There are many ways in which silica-supported membranes can be patterned[11,12], among them PDMS stamping[13], deposition by AFM tip[14], bilayer charge electrophoresis[15], and microlithography. Here, we use electron beam lithography (see **Figure 2** for schematic) to pattern metal barriers onto the silica support. These barriers are composed of thin, ~10nm high layers of chromium about 100nm wide and can be spaced as closely together as 500nm.

These chrome features serve as barriers to lipid lateral diffusion and can thus be used to restrict the movement of ligand proteins attached to the lipid head groups. With this technique, the area under a single cell can be divided into hundreds of discrete 2-dimensional corrals. The resulting perturbation to receptor organization on the cell surface can be thought of in multiple ways, frustrating receptor-ligand complex transport across the surface of the cell and also limiting the maximum number of receptor-ligand complexes that can appear in any single cluster. If the receptor targeted is a cytoskeletal effector, such restrictions may also have the effect of preventing the reorganization of F-actin morphology that might be seen if the receptor's travel across the cell membrane remained unhindered.

Planar supported lipid bilayers are easy to image and can be functionalized with a wide variety of biologically relevant proteins at precisely controllable densities. These features make the supported bilayer platform ideal for the study of the signaling implications of membrane receptor spatial organization.

Introduction References

1. Manz, B. N. & Groves, J. T. Spatial organization and signal transduction at intercellular junctions. *Nat. Rev. Mol. Cell Biol.* **11,** 342–352 (2010).

2. Mammen, M., Choi, S.-K. & Whitesides, G. M. Polyvalent Interactions in Biological Systems: Implications for Design and Use of Multivalent Ligands and Inhibitors. *Angew. Chem. Int. Ed.* **37,** 2754–2794 (1998).

3. Rio, A. del *et al.* Stretching Single Talin Rod Molecules Activates Vinculin Binding. *Science* **323,** 638–641 (2009).

4. Alberts, B. & Bray, D. *Molecular Biology of the Cell: the Lipid Bilayer.* (Garland Science, 1994).

5. Cremer, P. S. Formation and Spreading of Lipid Bilayers on Planar Glass Supports. *J. Phys. Chem. B* **103,** 2554–2559 (1999).

6. Groves, J. T., Wulfing, C. & Boxer, S. G. Electrical manipulation of glycan-phosphatidyl inositol-tethered proteins in planar supported bilayers. *Biophys. J.* **71,** 2716–2723 (1996).

7. Salafsky, J., Groves, J. T. & Boxer, S. G. Architecture and Function of Membrane Proteins in Planar Supported Bilayers: A Study with Photosynthetic Reaction Centers. *Biochemistry (Mosc.)* **35,** 14773–14781 (1996).

8. Nam, J.-M., Nair, P. M., Neve, R. M., Gray, J. W. & Groves, J. T. A Fluid Membrane-Based Soluble Ligand-Display System for Live-Cell Assays. *ChemBioChem* **7,** 436–440 (2006).

9. Nye, J. A. & Groves, J. T. Kinetic control of histidine-tagged protein surface density on supported lipid bilayers. *Langmuir ACS J. Surf. Colloids* **24,** 4145–4149 (2008).

10. Gureasko, J. *et al.* Membrane-dependent signal integration by the Ras activator Son of sevenless. *Nat. Struct. Mol. Biol.* **15,** 452–461 (2008).

11. Groves, J. T., Ulman, N. & Boxer, S. G. Micropatterning Fluid Lipid Bilayers on Solid Supports. *Science* **275,** 651–653 (1997).

12. Groves, J. T. & Boxer, S. G. Micropattern formation in supported lipid membranes. *Acc. Chem. Res.* **35,** 149–157 (2002).

13. Jennifer S. Hovis, S. G. B. Patterning Barriers to Lateral Diffusion in Supported Lipid Bilayer Membranes by Blotting and Stamping. *Langmuir* **16,** (2000).

14. Carlson, J. W., Bayburt, T. & Sligar, S. G. Nanopatterning Phospholipid Bilayers. *Langmuir* **16,** 3927–3931 (2000).

15. Groves, J. T., Boxer, S. G. & McConnell, H. M. Electric field-induced reorganization of two-component supported bilayer membranes. *Proc. Natl. Acad. Sci.* **94,** 13390–13395 (1997).

Introduction Figures

Figure 1. ***A typical phospholipid (top) and some common phospholipid head groups (bottom).***

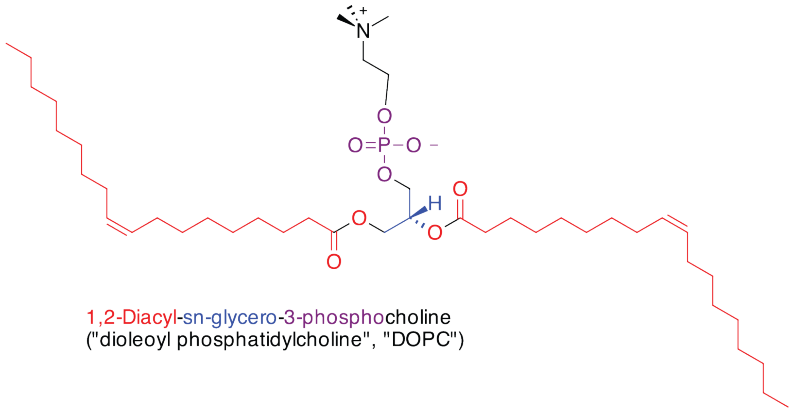

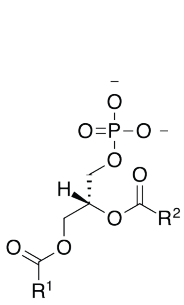
phosphatidic acid

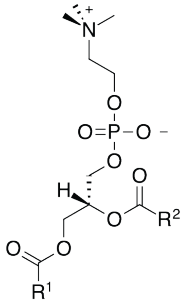
phosphatidylcholine

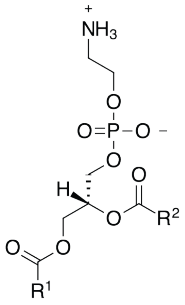
phosphatidylethanolamine

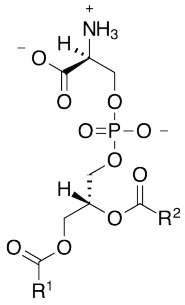
phosphatidylserine

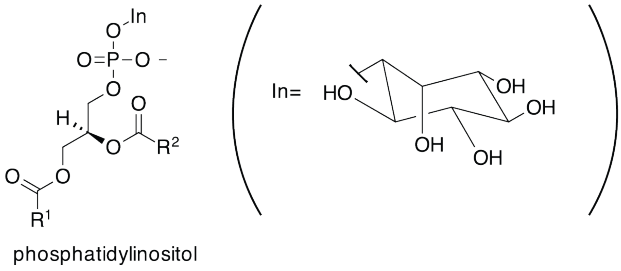

phosphatidylinositol

Table 1. *Saturated Fatty acids*

Common name	Chemical structure	*C:D**
Caprylic acid	$CH_3(CH_2)_6COOH$	8:0
Capric acid	$CH_3(CH_2)_8COOH$	10:0
Lauric acid	$CH_3(CH_2)_{10}COOH$	12:0
Myristic acid	$CH_3(CH_2)_{12}COOH$	14:0
Palmitic acid	$CH_3(CH_2)_{14}COOH$	16:0
Stearic acid	$CH_3(CH_2)_{16}COOH$	18:0
Arachidic acid	$CH_3(CH_2)_{18}COOH$	20:0
Behenic acid	$CH_3(CH_2)_{20}COOH$	22:0
Lignoceric acid	$CH_3(CH_2)_{22}COOH$	24:0
Cerotic acid	$CH_3(CH_2)_{24}COOH$	26:0

*C=the number of carbons in the chain, D=the number of C=C double bonds in the chain

Table 2. *Unsaturated Fatty acids*

Common name	Chemical structure	Δ^{x**}	*C*:*D*
Myristoleic acid	$CH_3(CH_2)_3$**CH=CH**$(CH_2)_7COOH$	*cis*-Δ^9	14:1
Palmitoleic acid	$CH_3(CH_2)_5$**CH=CH**$(CH_2)_7COOH$	*cis*-Δ^9	16:1
Sapienic acid	$CH_3(CH_2)_8$**CH=CH**$(CH_2)_4COOH$	*cis*-Δ^6	16:1
Oleic acid	$CH_3(CH_2)_7$**CH=CH**$(CH_2)_7COOH$	*cis*-Δ^9	18:1
Elaidic acid	$CH_3(CH_2)_7$**CH=CH**$(CH_2)_7COOH$	*trans*-Δ^9	18:1
Vaccenic acid	$CH_3(CH_2)_5$**CH=CH**$(CH_2)_9COOH$	*trans*-Δ^{11}	18:1
Linoleic acid	$CH_3(CH_2)_4$**CH=CH**CH_2**CH=CH**$(CH_2)_7COOH$	*cis,cis*-Δ^9,Δ^{12}	18:2
Linoelaidic acid	$CH_3(CH_2)_4$**CH=CH**CH_2**CH=CH**$(CH_2)_7COOH$	*trans,trans*-Δ^9,Δ^{12}	18:2
α-Linolenic acid	CH_3CH_2**CH=CH**CH_2**CH=CH**CH_2 **CH=CH**$(CH_2)_7COOH$	*cis,cis,cis*-$\Delta^9,\Delta^{12},\Delta^{15}$	18:3
Arachidonic acid	$CH_3(CH_2)_4$**CH=CH**CH_2**CH=CH**CH_2**CH=CH**CH_2**CH=CH**$(CH_2)_3COOH$	*cis,cis,cis,cis*-$\Delta^5\Delta^8,\Delta^{11},\Delta^{14}$	20:4
Eicosapentaenoic acid	CH_3CH_2**CH=CH**CH_2**CH=CH**CH_2 **CH=CH**CH_2**CH=CH**CH_2**CH=CH** $(CH_2)_3COOH$	*cis,cis,cis,cis,cis*-$\Delta^5,\Delta^8,\Delta^{11},\Delta^{14},\Delta^{17}$	20:5
Erucic acid	$CH_3(CH_2)_7$**CH=CH**$(CH_2)_{11}COOH$	*cis*-Δ^{13}	22:1
Docosahexaenoic acid	CH_3CH_2**CH=CH**CH_2**CH=CH**CH_2 **CH=CH**CH_2**CH=CH**CH_2**CH=CH** CH_2**CH=CH**$(CH_2)_2COOH$	*cis,cis,cis,cis,cis,cis*-$\Delta^4,\Delta^7,\Delta^{10},\Delta^{13},\Delta^{16},\Delta^{19}$	22:6

**This notation signifies a double bond starting at the carbon x atoms away from the carboxylic acid carbon.

Figure 1. (Next page) *Chromium grid fabrication process flow.* A. A negative electron-beam resist is spin-coated onto a clean glass substrate. B. A layer of conductive material, such as metal or a conducting polymer, is deposited atop the resist. C. The areas of resist where chrome coverage is desired are exposed with an electron beam. D. The conductive layer is stripped and the exposed areas of resist are dissolved in developer fluid. F. ~10nm of chromium is deposited atop the entire surface by electron beam or thermal evaporation. G. The remaining resist and the chrome above it are lifted off in resist solvent. H. The glass surface is activated with UV rays or piranha wash and small lipid vesicles are deposited atop the clean surface to fuse and form a lipid bilayer.

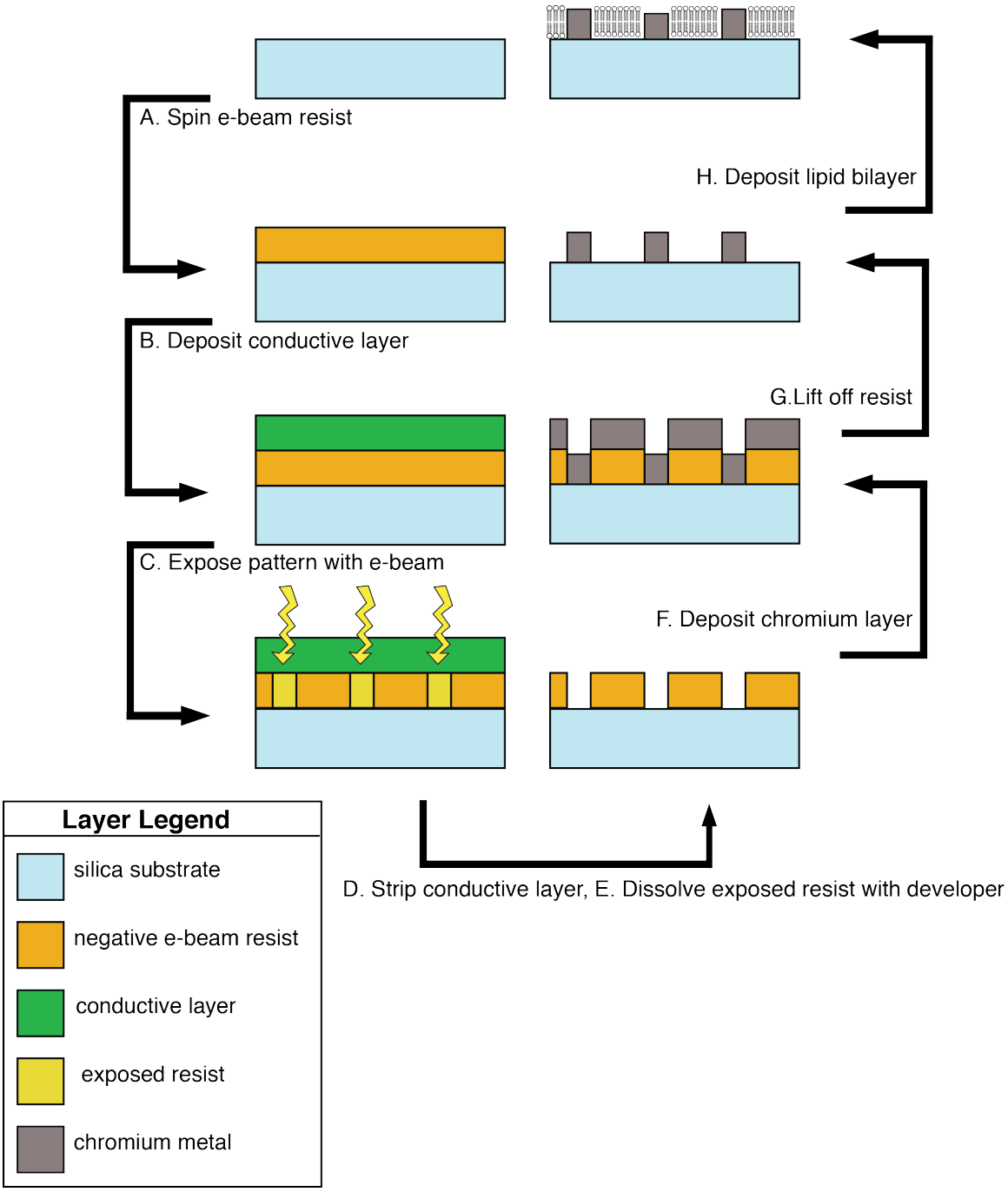
A. Spin e-beam resist
B. Deposit conductive layer
C. Expose pattern with e-beam
D. Strip conductive layer, E. Dissolve exposed resist with developer
F. Deposit chromium layer
G.Lift off resist
H. Deposit lipid bilayer
Layer Legend
silica substrate
negative e-beam resist
conductive layer
exposed resist
chromium metal

Chapter 1

Pharmaceutical Inhibition of EphA2-Mediated Contractility in Invasive Breast Cancer Cells on Ephrin-A1-Functionalized Planar Supported Lipid Bilayer

Abstract

EphA2-ephrin-A1 signaling is misregulated in many types of cancer, and abnormal regulation of actomyosin contractile ability is associated with the hypermotility exhibited by cancer cells with high invasive potential. Here we demonstrate and replicably quantify pharmaceutical curtailment of EphA2-dependent ROCK-mediated actomyosin contractility exhibited by the MDA-MB-231 line of invasive breast cancer cells upon contact with fluid, ephrin-A1 functionalized planar supported lipid bilayers and show that this inhibition leads to differential outcomes with regard to cell membrane recruitment of the metalloprotease ADAM10, a downstream effector protein of EphA2.

Introduction

The Eph family of receptors constitutes the largest known family of receptor tyrosine kinases. Found on the surfaces of cells, Ephs are transmembrane proteins with an extracellular ligand-binding domain and a juxtamembrane intracellular kinase domain[1]. Their intracellular portion also contains a sterile alpha motif domain and a PDZ-binding domain, both of which can serve as binding sites for downstream effector proteins. Eph's ligands are the ephrins, cell-surface proteins that may be GPI-bound (as in ephrin-As) or transmembrane (as in ephrin-Bs). There are nine mammalian EphAs, (EphA1-EphA8 and Eph10) which preferentially bind ephrin-As (ephrins-A1-A6), and five EphBs (EphB1-EphB4 and EphB6), which tend to bind ephrin-Bs (ephrins-B1-B3)[2], although certain cross-class interactions are also possible[3]. In normally-functioning biological systems, cell-cell interaction events featuring various Eph/ephrin combinations serve as localization guidance signals, triggering either cell-cell repulsion or adhesion, depending on the nature and duration of the binding. In this way, Eph/ephrin signaling plays a vital role in maintaining proper segregation of different tissue types during embryonic development[4].

The classical model of Eph signaling begins when an Eph receptor on one cell surface binds to a complementary ephrin on another cell surface. The resulting receptor-ligand complex presents a surface which can bind with another such complex to form a hetero-tetradimer. It is this dimer that is the smallest functional Eph signaling unit: dimerization forces the two intracellular kinase domains into close proximity with one another, allowing them to keep each other phosphorylated despite the presence of membrane-proximal phosphatases[5]. Heterodimers can then interact with each other to form higher-order Eph oligomers. Eph clusters formed in this way can serve as docking platforms for cytoplasmic signaling effectors[6–8]. As one might expect from Eph's status as a regulator of cell adhesion and repulsion, the activation pathway results in the remodeling of the cytoskeleton through small Rho-family GTPase signaling; in EphAs, this is thought to be mediated by the guanine nucleotide exchange factor ephexin[9–11].

Attenuation of this signaling cascade eventually occurs when phosphorylated Eph domains lead to the recruitment of cytoplasmic sheddases, which cleave ephrin *in trans* and enable endocytotic removal of Eph receptor from the cell membrane[6,12], thus facilitating Eph-mediated cell-cell repulsion. On the other hand, underphosphorylation of Eph receptors can prevent this attenuation from occurring, leading to Eph-mediated cell-cell adhesion instead. Such underphosphorylation can be caused by expression of kinase-deficient Eph variants or by trans-auto-phosphorylation-inhibiting interactions between Ephs and ephrins on the surface of the same cell[13].

Cancer cells often exhibit increased levels of Eph expression and alterations in function which have been observed to foster pathological behaviors such as tumor cell

migration and segregation[14]. Particularly notorious is EphA2, whose abnormal expression has been observed to correlate with poor prognosis and high malignancy in tumors and is associated with malignant breast and prostate cancers, particularly those of the highly aggressive basal phenotype. In many cancer cells, high EphA2 levels have been seen in conjunction with low levels of ephrin-dependent activity.

Myosin is a motor protein that uses chemical energy derived from ATP hydrolysis to power its ability to "walk" its actin-binding domain towards the barbed end of an actin filament. Although over a dozen different classes of myosin have been discovered, by far the largest is Class II[15]. Myosin II is a hexameric protein composed of two heavy chains and four light chains. Two of the four light chains, called essential light chains, are thought to play a role in stabilizing the lever arm formed by myosin's head during the force-generating step of the myosin activity cycle[16]. The other two light chains are called regulatory light chains and promote myosin's catalytic activity while phosphorylated. The heavy chains are made up of an N-terminal "head" region, which contains an actin binding domain and a catalytic ATP-binding domain, a "neck" region, each of which is host to myosin's two light chains, and a long "tail" region, which coils together with the second heavy chain's tail to form a helical superstructure[17].

Myosin II plays a crucial role in cell migration and adhesion via its generation of contractile force. Two myosin units can form a dimer through adhesive interactions between their two tail domains, creating a superstructure with myosin heads at both ends. These dimers can further aggregate to form filaments of myosin. When this bipolar superstructure crossbridges between two anti-parallel actin filaments, forcible conformation changes in the myosin head driven by ATP hydrolysis can induce unanchored actin filaments to slide towards another and can produce tension in anchored actin filaments[18].

Myosin's propensity to act on the cytoskeleton is regulated in part by the balance between the activity of myosin light chain (MLC) kinases, which serve to catalyze the phosphorylation of myosin's regulatory light chain, and the activity of myosin light chain phosphatases, which catalyze their dephosphorylation. This balance is spatially and temporally modulated by the serine/threonine kinase known as Rho-kinase (ROCK). ROCK is a downstream effector of the Rho family of small GTPases. A member of the DMPK (dystrophia myotonica-protein kinase) family in the AGC protein kinase group, the ROCK subfamily consists of two isoforms, ROKα and ROKβ, which modulate the assembly of actomyosin filaments. Rho/ROCK signaling plays a crucial role in the generation of cytoskeletal contractile force in response to extracellular biochemical and mechanical stimuli, and is a known mediator of many important cellular processes, including stress fiber assembly, contact-dependent cell-cell repulsion[19], and cell motility[20].

Abnormal regulation of Rho/ROCK signaling activity has been observed to correlate with invasiveness and metastatic potential in many instances of cancer[21]. Factors

potentially contributing to this dysregulation have been identified on many levels of the pathway, including overexpression and hyperactivation of Rho GTPases[22–25], overexpression of membrane-bound receptor tyrosine kinases[26], altered ROCK subcellular localization[27, 28], ROCK overexpression[29], and somatic mutations that increase ROCK's kinase activity[10, 11].

Once activated by binding to GTP-Rho, ROCK can phosphorylate a number of cytoskeletal effector proteins. Of particular relevance to its ability to regulate actomyosin contractility is its ability to promote the phosphorylation of myosin's regulatory light chain, which increases myosin's affinity for actin filament binding. In addition to having the ability to phosphorylate MLC2 directly[32], ROCK's kinase activity can also de-activate the myosin-targeting subunit of myosin phosphatase, thus preventing myosin phosphatase from dephosphorylating the myosin regulatory light chain[33, 34]. In addition to promoting myosin association with F-actin in this way, ROCK also promotes contractile force transduction through LIM kinase-mediated phosphorylative de-activation of the actin depolymerizing protein cofilin[35, 36]. While active, cofilin competes with myosin for the same F-actin binding sites[37].

In this investigation, we used an ephrin-A1-functionalized supported lipid bilayer to investigate the ligand-dependent contractility response induced in MDA-MB-231 cancer cells upon contact with this surface (**Figure 1**). This technique involves the use of a planar silica support as a substrate for the formation of a lipid bilayer, which is created when small lamellar vesicles settle upon the silica surface, rupture, and fuse with one another[38]. Bilayers thus created can be functionalized with biologically relevant molecules using a variety of different linkage schemes. Here, we incorporated into the synthetic bilayer a fraction of lipid molecules with biotinylated heads. To this bilayer, we add streptavidin, which binds to the bilayer and provides an anchor-point for biotinylated, dye-conjugated recombinant protein that consists of F_c of human IgG fused to two ephrin-A1 receptor-binding domains. When bound to a surface that is allowed to interact with a cell, this dimeric ligand functionality is a robust activator of cell membrane EphA2, as quantified by receptor degradation[39].

Results and Discussion

EphA2 receptor stimulation by contact with a planar surface of ephrin-A1 results in the formation of cell membrane ephrin-A1-EphA2 complexes. Initially distributed evenly under the cell, these complexes begin to assemble into punctate clusters which are eventually transported towards the center of the cell-substrate interface to form a planar assembly of Eph/ephrin complexes about 3 microns in diameter. Under typical experimental conditions, the assembly of this central complex is complete in 45 minutes to an hour. During this time, the areas under the cell coincident with the localization of Eph/Ephrin clusters also correspond to the only areas of close cell-substrate contact; the

spread morphology that the cells adopt upon first encountering and clustering ligand then graduates to a rounded morphology as the area of cell contact with the substrate shrinks to follow the centripetal motion of the complex clusters (**Figure 2**). Phalloidin staining shows that the central ephrin-A1 accumulation is surrounded by a ring of perimembrane F-actin (**Figure 3**).

Notably, the formation of this central region of contact is accompanied by the recruitment to the contact area of the disintegrin and metalloprotease ADAM10, whose cleavage of ephrin-A1 *in trans* has been shown to mediate EphA2-dependent cell repulsion in tissues, and as might be expected, the inhibition of ADAM10 protease activity has also been shown to decrease the degree of EphA2 degradation seen by western blotting cell lysate after supported bilayer ephrin-A1 stimulation. ADAM10 recruitment to the cell membrane is abrogated when the cell is mechanically prevented from forming this central contact, suggesting that the recruitment is at least partially dependent on the cell's ability to remodel its cytoskeletal architecture in response to ephrin stimulation.

Previous investigations across a variety of breast cancer cell lines have found that the degree to which cells on ephrin-A1 functionalized bilayers form these central areas of high Eph/ephrin complex density correlates well to the degree of invasive potential that these cell lines variously exhibit, as measured by matrigel invasion assays. Interestingly, this correlation is stronger than that of EphA2 overexpression with invasive potential, suggesting that the degree to which this contractile behavior occurs depends on factors besides the mere number of Eph receptors present on the cell membrane[39].

To test the hypothesis that Eph/ephrin complex receptor transport is dependent on Rho-mediated actomyosin contractility, we treated cells with calyculin A, a serine/threonine phosphatase inhibitor whose inactivation of myosin light-chain phosphatase results in hyperactivation of actomyosin contractility[40–42]. Cells cultured on 1:10 cRGD:Alexa Fluor-647-ephrin-A1 functionalized bilayers in 1nM calyculin A were observed to exhibit significantly higher degrees of interfacial ephrin-A1-647 aggregation as measured by peak radial values of fluorophore label density (**Figure 4**).

To further test the hypothesis that ephrin-A1 radial transport under bilayer-stimulated cells is contractility-regulated, we used Rho-kinase selective inhibitor Y-27632 to abrogate the effects of ROCK signaling on cytoskeletal morphology. Y-27632 binds ROCK competitively with ATP. When cells were cultured for one hour on ephrin-A1 functionalized bilayers in the presence of increasing doses of Y-27632, the inhibitor-dosed cells showed a marked decrease in their ability to transport Eph/ephrin complexes across the plane. Ephrin-A1 density under these cells resembled rosettes, with peak radial ephrin-A1 densities occurring further from the cell footprint center with increasing inhibitor dose (**Figure 5A-I**). A similar experiment using a bilayer functionalized with cyclic RGD peptide as well as ephrin-A1 revealed that when cell footprint contact areas were roughly equal,

the total ephrin-A1 density accumulated under the cell was significantly lower in ROCK-inhibited cells (**Figure 5J-R**).

To investigate whether ROCK inhibition-mediated Eph receptor transport abrogation affected signaling pathways downstream of Eph, we stimulated ROCK-inhibitor-dosed cells on ephrin-A1 bilayers and stained them for Eph receptor and for ADAM10, and visualized the interfacial densities of antibody-conjugated fluorophore with total internal reflection (TIRF) microscopy. As might be expected, the radial density profiles of EphA2 stain intensity (**Figure 6B**) vary with ROCK inhibitor dosage in much the same way that ephrin-A1 densities do (**Figure 5A**); higher dosing leads to average peak radial fluorophore density values shifted further away from the centroid of the cell/bilayer interface footprint. In contrast, ADAM10 stain profiles (**Figure 6A**), rather than appearing as "rings" of radius increasing with ROCK inhibitor dose as EphA2 and ephrin-A1 densities do, show that central aggregation of ADAM10 occurs to a greater or lesser extent depending on the degree of EphA2 agglomeration observed at the center of the cell footprint area. Indeed, total integrated ADAM10 TIRF intensity levels measured within a 12-micron radius of the apparent center of the cell/bilayer interface were seen to decrease progressively with increasing dosage of ROCK inhibitor (**Figure 6D**), though no consistent inhibitor dose trend is seen to affect EphA2 stain TIRF intensity levels (**Figure 6C**). Pearson's correlation coefficient of signal intensity variations in the two imaging channels (**Figure 6E**) shows that ROCK inhibition progressively decreases the degree of association between perimembrane ADAM10 and EphA2, suggesting that signals downstream of EphA2 may be modulated by the extent of this process.

Taken together, these results indicate that the process of ephrin-A1-dependent EphA2 large cluster formation is driven by the effects of ROCK signaling on the shape of the actin cytoskeleton. This is not unexpected, as EphA2/ephrin-A1 cell repulsion interactions depend on adhesion area reduction and cell process retraction that is mediated by Rho-dependent actomyosin contractility[43]. As previously mentioned, the degree of bilayer-stimulation dependent interfacial EphA2-ephrin-A1 aggregation across various cancer cell lines correlates more strongly with their invasiveness than would be expected if this process were dependent upon EphA2 expression levels alone. The results of this investigation suggest that differentials in the degrees of Rho-ROCK signal activity that these various cell lines exhibit would also be expected to contribute to variations in their tendencies to aggregate Eph/ephrin complexes. This squares well with the results of recent studies on the migration and invasion mechanisms of the MDA-MB-231 cell line: two- and three-dimensional matrigel invasion assays show that these cells depend on contractile activity at the cell rear to drive locomotion through the matrix[44], and EphA2-mediated recruitment of metalloprotease serves to increase MDA-MB-231 cells' tendency for individual cell invasion in both in vivo and in vitro studies. This shift is effected through an increase in Rho-contractility signaling caused by EphA2 cleavage and internalization[45].

Research into the possible therapeutic applications of pharmaceutical inhibition of actomyosin contractility faces many challenges. Rho/ROCK and associated downstream signaling events are potentially useful targets for pharmacologic intervention, but the effectiveness of such measures varies from case to case. Although ROCK inhibitors have been successfully used to decrease tumor cell metastasis in some animal models[46], other investigations have shown ROCK inhibition to increase the rate of cancer cell chemoresistance emergence[47] and even to promote invasiveness in some tumors[47]. In order to safely and efficaciously use pharmacological ROCK inhibition, it will be necessary to develop assays by which the possible inhibitor susceptibility of a patient's tumor sample can be gauged. In this study, we have shown that the functionalized supported lipid bilayer platform can be used with as few as 200 cells to replicably quantify cancer cell response to different levels of pharmacological inhibition of ROCK activity.

Materials and Methods

Supported Membrane Preparation

The desired lipids were mixed in a chloroform solution and then the chloroform was evaporated using a rotary evaporator. The lipids were thoroughly dried under a stream of N_2 and hydrated with 1.5 mL of DI water. The hydrated lipids were then extruded through 100 nm-sized polycarbonate pore filters and stored at 4°C. Fluid bilayers were made from vesicles containing DOPC (1,2-dioleoyl-sn-glycero-3-phosphocholine), and 0.1% biotin-DPPE (1,2-dipalmitoyl-sn-glycero-3-phosphoethanolamine-N-(cap biotinyl)). All lipids were acquired from Avanti Polar Lipids, Inc., Alabaster, AL. Vesicles were allowed to warm to room temperature and mixed in a 1:3 ratio with 1× phosphate-buffered saline (PBS; Sigma-Aldrich, Inc., Saint Louis, MO) to a final concentration of 1 mg/ml. For experiments performed in 96-well plates, each well was pre-treated with 1 M NaOH for 1 hour and then thoroughly rinsed with DI water. 100μL of the lipid vesicle solution in PBS was then added to each well and excess vesicles were subsequently rinsed. For experiments performed on microscopic cover glass, substrates were cleaned using a piranha etching protocol (H_2SO_4 and H_2O_2 mixed in a 3:1 ratio) for 15 min, and then rinsed and dried under a stream of N_2. Lipid vesicle solutions were then spread over these substrates. The resulting lipid-bilayer functionalized substrate was immersed in PBS and sealed in an Attofluor cell chamber (Invitrogen Corp., Carlsbad, CA). In order to facilitate vesicle rupture and spreading, lipid solutions were extruded through 100 and 30 nm-sized pore filters and all solutions and substrates were heated to 50°C.

Surface Functionalization

After lipid bilayer deposition, substrates were incubated for 45 minutes with a 0.01% bovine serum albumin (BSA; Sigma-Aldrich, Inc.) solution to minimize non-specific protein adsorption. The supported membranes were then incubated with a 17 nM solution of streptavidin (Fisher Scientific, Pittsburgh, PA) for 45 minutes. RGD-functionalized

supported membranes were generated by incubating streptavidin-functionalized membranes with a cyclic peptide [Arg-Gly-Asp-d-Phe-Lys (Biotin-PEG-PEG)] where PEG = 8-Amino-3,6-Dioxaoctanoic Acid (PCI-3697-PI, Peptides International, Louisville, KY) at the molar concentrations indicated.

In all cell experiments, the PBS solutions were exchanged by rinsing the substrate with DMEM cell media (GIBCO) at 37°C. Cells were then added to the substrates and allowed to engage and interact with the surface at the conditions indicated.

Optical Microscopy

Images were collected on Nikon Eclipse TE2000-E and TE300 inverted microscopes with mercury arc lamps for epifluorescence illumination and 12 V, 100 W halogen lamps for bright field illumination. Total internal reflection fluorescence (TIRF) illumination was provided using a krypton/argon ion laser for 647 nm excitation, and an argon ion laser (Stabilite 2018 and Model 177 respectively, both from Spectra-Physics, Mountain View, CA) for 488 nm excitation. All epifluorescence microscope images were taken with a Quantix CCD camera and TIRF microscope images were taken using a Cascade 512B EMCCD camera. All cameras were purchased from Roper Scientific, Ottobrunn, Germany. MetaMorph (Molecular Devices Corp., Downington, PA) software was used to drive microscope and collect the images. Alexa Fluor 647 was imaged using a Cy5 filter cube and Alexa Fluor 488 and was imaged using an NBD/HPTS filter cube.

Reflection Interference Contrast Microscopy

(RICM) images were collected using a dedicated RICM filter cube. All filter cubes were acquired from Chroma Technology Corp., Rockingham, VT. Alexa Fluor 647 Ephrin-A1 and EGFP-actin tracking was performed using a DualView (Photometrics, Tucson, AZ) image splitter fitted with a dual-band pass emission filter interposed between the body of the microscope and the camera.

Quantitative TIRF Microscopy

In order to account for differences in illumination intensity across the visualized area between 488 nm and 647 nm laser TIRF excitation, a calibration bilayer was used. The calibration bilayer contained 99.9% DOPC and 0.1% biotin-modified DHPE and was incubated for 45 minutes with a 1:1 mixture of Alexa Fluor 488 streptavidin and Alexa Fluor 647 streptavidin, each with a F/P ratio of 2. The bilayer was then rinsed with PBS. Several unique areas of the calibration bilayer were imaged in the 488 nm and 647 nm excitation channels. An average, background-subtracted image was obtained for each channel. Background-subtracted sample images from each channel were divided by the average background-subtracted calibration image for the same channel, yielding sample images with normalized illumination intensities that could be quantitatively compared between the 2 channels for the entire field of view. The ratio of signal from the ADAM10

channel to signal from the EphA2 channel was calculated independently for each cell. The Pearson's coefficient for these two channels was also calculated independently for each cell. These quantities were obtained using image analysis software package ImageJ.

Radial Transport Analysis

Bright field microscopy was used to determine the area occupied by each cell. The corresponding areas in the fluorescence channel were then analyzed using the Radial Profile plugin from ImageJ, yielding a plot of normalized fluorescence intensities versus radial distance from the cell center. Plots were then normalized for cell size and averaged. Least squares analysis was then performed on the average normalized radial distribution using Origin 7.0 (OriginLab, Northampton, MA), and the slope of the calculated line was used as a score for propensity to radially transport ephrin-A1.

Cell fixing and membrane permeabilization

For immunofluorescence experiments, cells were cultured on substrates for 1 hour. Cells were then rinsed with cold Dulbecco's PBS (Invitrogen Corp.) and fixed with 4% paraformaldehyde (EMD Chemicals, Inc., Gibbstown, NJ) in PBS (Invitrogen Corp.) for 12 minutes. When noted, cells were permeabilized with 0.1% Triton-X (EMD Chemicals, Inc.) in PBS for 5 minutes. Cells were then incubated overnight at 4°C in PBS containing 1% BSA to block non-specific antibody binding.

Cell Staining

After fixing, cells were stained for 40 minutes with primary antibodies against a variety of target molecules. F-actin was stained using phalloidin conjugated to Alexa Fluor 647 (Invitrogen Corp.), according to manufacturer protocols. For EphA2, and ADAM10 staining, cells were permeabilized before antibody addition. Anti-EphA2 antibody (sc-924) and anti-ADAM10 (sc-48400) antibodies were incubated at 2 μg/ml. After primary antibody incubation, excess antibody was rinsed away with PBS containing 1% BSA and isotype-matched secondary antibodies conjugated to either Alexa Fluor 488 or Alexa Fluor 647 (Invitrogen Corp.) were incubated at a concentration of 2μg/ml for 20-30 minutes. Excess secondary antibody was rinsed away with PBS.

Contractility Drugging

Cells were detached from cell culture flasks using trypsin-EDTA and incubated at 37°C for 2 hrs in media containing ROCK inhibitor Y-27632 (Sigma-Aldrich, Inc.) at concentrations ranging from 1-50 μM. Trypan blue staining and cell counting indicated no adverse effects in terms of cell viability under these conditions. Cells were cultured in drugged media for one hour on well plates containing Alexa Fluor 647-labeled ephrin-A1 functionalized supported bilayers. Cells were fixed, stained and imaged with epifluorescence or TIRF microscopy as described above. For myosin phosphatase inhibition, cells were cultured in

wells as above for 10 minutes, calyculin A (Cell Signaling, Inc., Beverly, MA) was added to wells to reach 1 nM concentration, and cells were incubated an additional 50 minutes before fixation.

Colocalization Analysis

After culturing cells on substrates for 1 hour, cells were fixed, cell membranes were permeabilized, and target molecules were stained and then imaged using TIRF microscopy as described above. Areas occupied by cells (20μm x 20μm in size) were chosen using bright field images. These same areas were designated as regions of interest in ImageJ and cropped for further analysis. To calculate the Pearson correlation coefficient, intensity of each pixel in the ADAM10 channel was plotted against pixel number. Similarly, intensity of each pixel in the EphA2 channel was plotted against pixel number. Least squares analysis was performed to fit a straight line to intensity values from each channel. The Pearson correlation coefficient was determined as the correlation coefficient between these 2 lines.

Cell Culture

Cells were provided by the Gray Lab (Lawrence Berkeley National Laboratory) and cultured using media, supplements, and conditions provided by the National Cancer Institute's Integrative Cancer Biology Program. The day of the experiments, cells were treated with trypsin-EDTA, centrifuged, resuspended in media, counted, and aliquoted as needed. Aliquots were kept in a 37°C, 5% CO_2, 100% humidity incubator until they were added to supported membranes.

References

1. Blume-Jensen, P. & Hunter, T. Oncogenic kinase signaling. *Nature* **411,** 355–365 (2001).

2. Gale, N. W. *et al.* Eph receptors and ligands comprise two major specificity subclasses and are reciprocally compartmentalized during embryogenesis. *Neuron* **17,** 9–19 (1996).

3. Himanen, J.-P. *et al.* Repelling class discrimination: ephrin-A5 binds to and activates EphB2 receptor signaling. *Nat. Neurosci.* **7,** 501–509 (2004).

4. Poliakov, A., Cotrina, M. & Wilkinson, D. G. Diverse roles of eph receptors and ephrins in the regulation of cell migration and tissue assembly. *Dev. Cell* **7,** 465–480 (2004).

5. Hubbard, S. R. Juxtamembrane autoinhibition in receptor tyrosine kinases. *Nat. Rev. Mol. Cell Biol.* **5,** 464–471 (2004).

6. Janes, P. W. *et al.* Adam Meets Eph: An ADAM Substrate Recognition Module Acts as a Molecular Switch for Ephrin Cleavage In trans. *Cell* **123,** 291–304 (2005).

7. Seiradake, E., Harlos, K., Sutton, G., Aricescu, A. R. & Jones, E. Y. An extracellular steric seeding mechanism for Eph-ephrin signaling platform assembly. *Nat. Struct. Mol. Biol.* **17,** 398–402 (2010).

8. Himanen, J. P. *et al.* Architecture of Eph receptor clusters. *Proc. Natl. Acad. Sci.* **107,** 10860–10865 (2010).

9. Hiramoto-Yamaki, N. *et al.* Ephexin4 and EphA2 mediate cell migration through a RhoG-dependent mechanism. *J. Cell Biol.* **190,** 461–477 (2010).

10. Sahin, M. *et al.* Eph-dependent tyrosine phosphorylation of ephexin1 modulates growth cone collapse. *Neuron* **46,** 191–204 (2005).

11. Shamah, S. M. *et al.* EphA receptors regulate growth cone dynamics through the novel guanine nucleotide exchange factor ephexin. *Cell* **105,** 233–244 (2001).

12. Janes, P. W. *et al.* Cytoplasmic Relaxation of Active Eph Controls Ephrin Shedding by ADAM10. *PLoS Biol* **7,** e1000215 (2009).

13. Halloran, M. C. & Wolman, M. A. Repulsion or adhesion: receptors make the call. *Curr. Opin. Cell Biol.* **18,** 533–540 (2006).

14. Nievergall, E., Lackmann, M. & Janes, P. W. Eph-dependent cell-cell adhesion and segregation in development and cancer. *Cell. Mol. Life Sci.* **69,** 1813–1842 (2012).

15. Sellers, J. R. Myosins: a diverse superfamily. *Biochim. Biophys. Acta BBA - Mol. Cell Res.***1496,** 3–22 (2000).

16. Ushakov, D. S. Structure and function of the essential light chain of myosin. *Biophysics* **53,** 505–509 (2008).

17. Bresnick, A. R. Molecular mechanisms of nonmuscle myosin-II regulation. *Curr. Opin. Cell Biol.***11,** 26–33 (1999).

18. Vicente-Manzanares, M., Ma, X., Adelstein, R. S. & Horwitz, A. R. Non-muscle myosin II takes centre stage in cell adhesion and migration. *Nat. Rev. Mol. Cell Biol.***10,** 778–790 (2009).

19. Kadir, S., Astin, J. W., Tahtamouni, L., Martin, P. & Nobes, C. D. Microtubule remodelling is required for the front–rear polarity switch during contact inhibition of locomotion. *J. Cell Sci.***124,** 2642–2653 (2011).

20. Parri, M. & Chiarugi, P. Rac and Rho GTPases in cancer cell motility control. *Cell Commun. Signal.* **8,** 23 (2010).

21. Kamai, T. *et al.* Significant association of Rho/ROCK pathway with invasion and metastasis of bladder cancer. *Clin. Cancer Res. Off. J. Am. Assoc. Cancer Res.* **9,** 2632–2641 (2003).

22. Burbelo, P., Wellstein, A. & Pestell, R. G. Altered Rho GTPase Signaling Pathways in Breast Cancer Cells. *Breast Cancer Res. Treat.* **84,** 43–48 (2004).

23. Clark, E. A., Golub, T. R., Lander, E. S. & Hynes, R. O. Genomic analysis of metastasis reveals an essential role for RhoC. *Nature* **406,** 532–535 (2000).

24. Vigil, D., Cherfils, J., Rossman, K. L. & Der, C. J. Ras superfamily GEFs and GAPs: validated and tractable targets for cancer therapy? *Nat. Rev. Cancer* **10,** 842–857 (2010).

25. Fritz, G., Just, I. & Kaina, B. Rho GTPases are over-expressed in human tumors. *Int. J. Cancer* **81,** 682–687 (1999).

26. Fang, W. B. *et al.* Overexpression of EPHA2 receptor destabilizes adherens junctions via a RhoA-dependent mechanism. *J. Cell Sci.* **121,** 358–368 (2008).

27. Dunlop, M. G. *et al.* Common variation near CDKN1A, POLD3 and SHROOM2 influences colorectal cancer risk. *Nat. Genet.* **44,** 770–776 (2012).

28. Nishimura, T. & Takeichi, M. Shroom3-mediated recruitment of Rho kinases to the apical cell junctions regulates epithelial and neuroepithelial planar remodeling. *Development* **135,** 1493–1502 (2008).

29. Lane, J., Martin, T. A., Watkins, G., Mansel, R. E. & Jiang, W. G. The expression and prognostic value of ROCK I and ROCK II and their role in human breast cancer. *Int. J. Oncol.* **33,** 585–593 (2008).

30. Forbes, S. A. *et al.* COSMIC (the Catalogue of Somatic Mutations in Cancer): a resource to investigate acquired mutations in human cancer. *Nucleic Acids Res.* **38,** D652–D657 (2010).

31. Greenman, C. *et al.* Patterns of somatic mutation in human cancer genomes. *Nature* **446,** 153–158 (2007).

32. Amano, M. *et al.* Phosphorylation and Activation of Myosin by Rho-associated Kinase (Rho-kinase). *J. Biol. Chem.* **271,** 20246–20249 (1996).

33. Kimura, K. *et al.* Regulation of Myosin Phosphatase by Rho and Rho-Associated Kinase (Rho-Kinase). *Science* **273,** 245–248 (1996).

34. Velasco, G., Armstrong, C., Morrice, N., Frame, S. & Cohen, P. Phosphorylation of the regulatory subunit of smooth muscle protein phosphatase 1M at Thr850 induces its dissociation from myosin. *FEBS Lett.* **527,** 101–104 (2002).

35. Zhang, Z. *et al.* Direct Rho-associated kinase inhibiton induces cofilin dephosphorylation and neurite outgrowth in PC-12 cells. *Cell. Mol. Biol. Lett.* **11,** 12–29 (2006).

36. Maekawa, M. *et al.* Signaling from Rho to the Actin Cytoskeleton Through Protein Kinases ROCK and LIM-kinase. *Science* **285,** 895–898 (1999).

37. Wiggan, O., Shaw, A. E., DeLuca, J. G. & Bamburg, J. R. ADF/Cofilin Regulates Actomyosin Assembly through Competitive Inhibition of Myosin II Binding to F-Actin. *Dev. Cell* **22,** 530–543 (2012).

38. Groves, J. T., Ulman, N. & Boxer, S. G. Micropatterning Fluid Lipid Bilayers on Solid Supports. *Science* **275,** 651–653 (1997).

39. Salaita, K. *et al.* Restriction of Receptor Movement Alters Cellular Response: Physical Force Sensing by EphA2. *Science* **327,** 1380–1385 (2010).

40. Suzuki, A. & Itoh, T. Effects of calyculin A on tension and myosin phosphorylation in skinned smooth muscle of the rabbit mesenteric artery. *Br. J. Pharmacol.* **109,** 703–712 (1993).

41. Fujiki, H. *et al.* Mechanisms of action of okadaic acid class tumor promoters on mouse skin. *Environ. Health Perspect.* **93,** 211–214 (1991).

42. Suganuma, M. *et al.* Calyculin A, an inhibitor of protein phosphatases, a potent tumor promoter on CD-1 mouse skin. *Cancer Res.* **50,** 3521–3525 (1990).

43. Parri, M. *et al.* EphrinA1 Activates a Src/Focal Adhesion Kinase-mediated Motility Response Leading to Rho-dependent Actino/Myosin Contractility. *J. Biol. Chem.* **282,** 19619–19628 (2007).

44. Poincloux, R. *et al.* Contractility of the cell rear drives invasion of breast tumor cells in 3D Matrigel. *Proc. Natl. Acad. Sci. U. S. A.* **108,** 1943–1948 (2011).

45. Sugiyama, N. *et al.* EphA2 cleavage by MT1-MMP triggers single cancer cell invasion via homotypic cell repulsion. *J. Cell Biol.* **201,** 467–484 (2013).

46. Ying, H. *et al.* The Rho kinase inhibitor fasudil inhibits tumor progression in human and rat tumor models. *Mol. Cancer Ther.* **5,** 2158–2164 (2006).

47. Street, C. A. *et al.* Pharmacological inhibition of Rho-kinase (ROCK) signaling enhances cisplatin resistance in neuroblastoma cells. *Int. J. Oncol.* **37,** 1297–1305 (2010).

Chapter 1 Figures

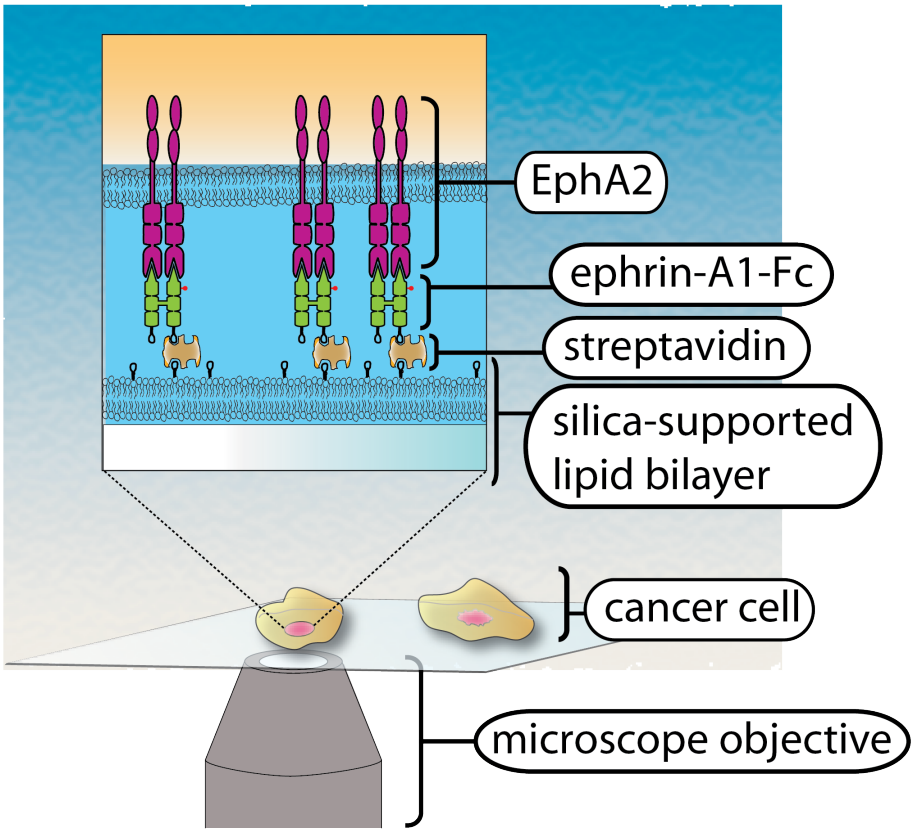

Figure 1. *Experimental setup: inverted fluorescence microscopy on functionalized, supported lipid bilayer.* When deposited under water onto a clean silica surface, vesicles of DOPC with 0.1% biotinylated DPPE fuse into a fluid bilayer. When streptavidin is added to the bilayer chamber, it binds to biotinylated lipids and serves as a linking anchor for a fluorescently labeled recombinant protein composed of two receptor-binding domains of ephrin-A1 fused to IgG F_c. The ligand-functionalized bilayer can now serve as an activating surface for EphA2-expressing breast cancer cells, which bind ligand on the surface and transport the EphA2/ephrin-A1 complexes laterally towards the center of each cell-bilayer interface. The resulting changes in surface ligand density are visualized from an air objective located below the water chamber.

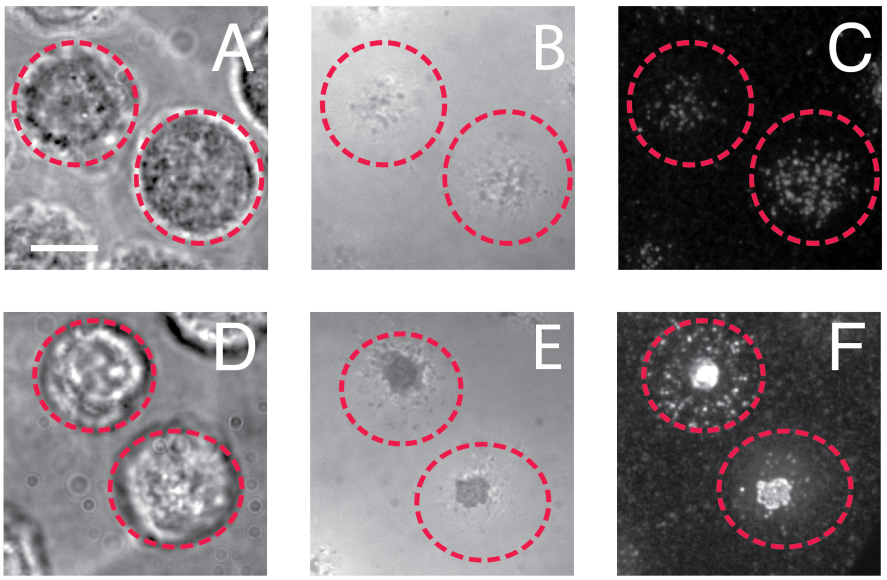

Figure 2. *Ephrin-A1 colocalizes with close cell-bilayer contact points in the first hour of ephrin-A1 bilayer stimulation.* MDA-MB-231 cells cultured at 37°C on Alexa Fluor 647-ephrin-A1-functionalized bilayers for 10 minutes **(A-C)** and for one hour **(D-F)** imaged with bright field **(A, D)**, RICM **(B, E)** and epifluorescence **(C, F).** Scale bar: 10μm. At ten minutes stimulation on the bilayer, punctate clusters of bilayer ephrin-A1 are seen to form under the cell. At one hour stimulation, subcellular ephrin-A1 is aggregated into a central macrocluster ~3μm in diameter.

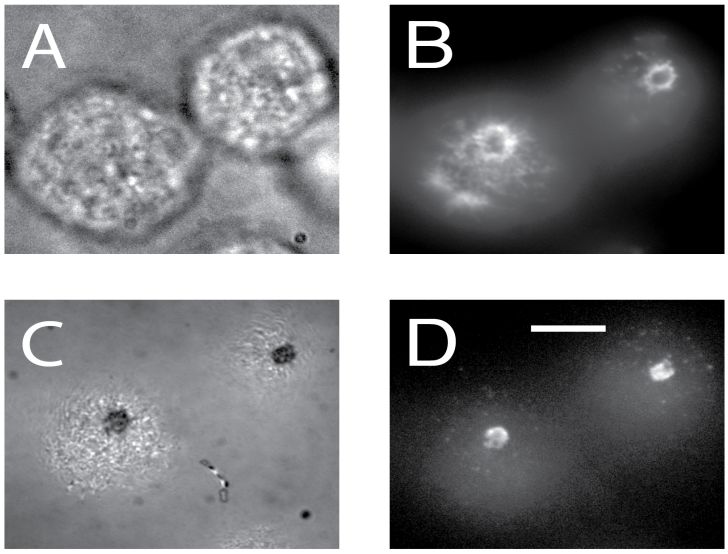

Figure 3. *An F-Actin annulus lines the periphery of centralized ephrin-A1 macrocluster.* Cells cultured for 1 hour on Alexa Fluor 350-ephrin-A1 functionalized bilayers and stained with Alexa Fluor 647-phalloidin show the formation of a ring-shaped actin feature that surrounds both the accumulations of ephrin-A1 under each cell and the region of each cell's closest contact with the substrate. A: Bright field, B: epifluorescence image of phalloidin-647, C: RICM, D: epifluorescence image of ephrin-A1-350. Scale bar: 10μm.

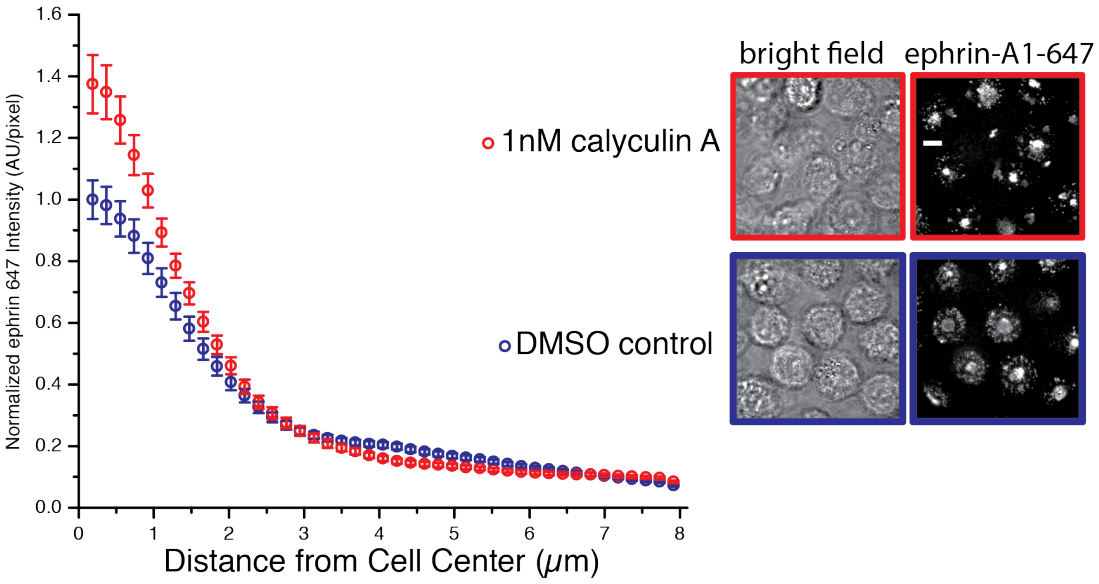

Figure 4. *Biochemical MLC phosphatase inhibition enhances subcellular centripetal transport of ephrin-A1.* Drugged cells cultured for 1 hour on 10:1 ephrin-A1: cRGD functionalized bilayers exhibit substantial increase in their ability to form tight central aggregations of Alexa Fluor 647-labeled ephrin-A1 at the cell/bilayer planar interface. Scale bar: 10μm. Calyculin data set n=84 cells, DMSO control data set n=66 cells.

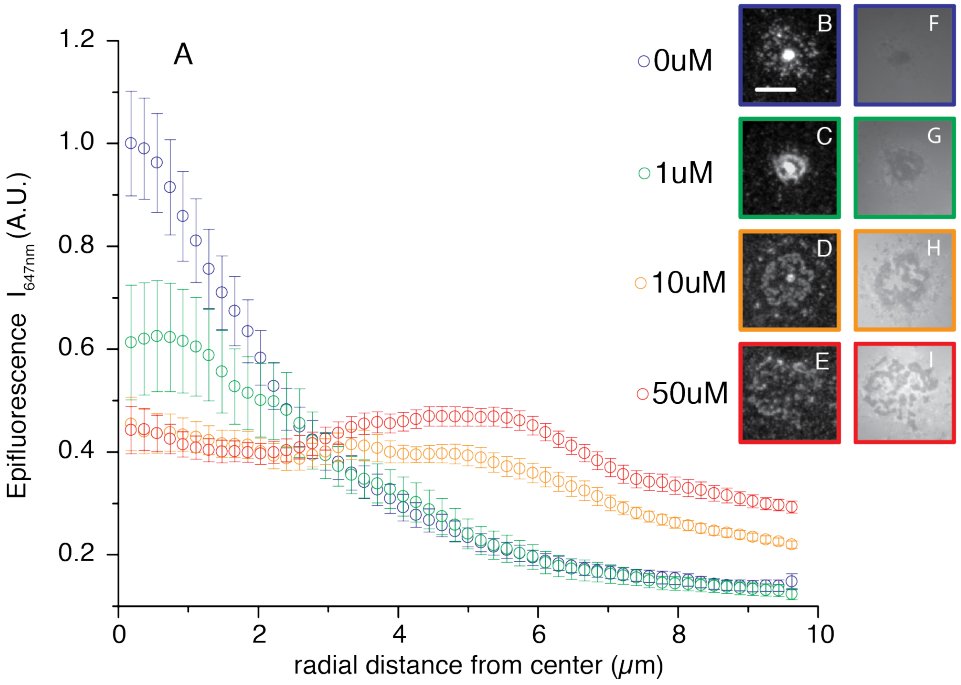
A
0uM
1uM
10uM
50uM
B
F
C
G
D
H
E
I
Epifluorescence I_{647nm} (A.U.)
radial distance from center (μm)

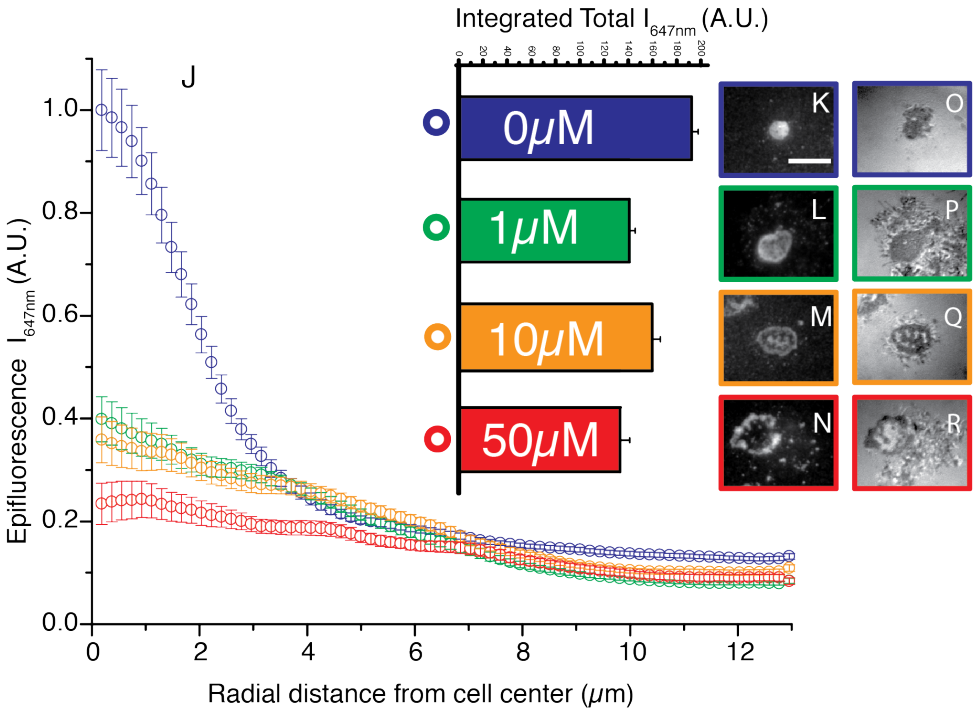
J
Integrated Total I_{647nm} (A.U.)
0μM
1μM
10μM
50μM
K
O
L
P
M
Q
N
R
Epifluorescence I_{647nm} (A.U.)
Radial distance from cell center (μm)

Figure 5. *Biochemical ROCK inhibition hinders subcellular centripetal transport of ephrin-A1.* Drugged cells cultured for 1 hour on bilayers functionalized with ephrin-A1 **(A-I)** and bilayers functionalized with both ephrin-A1 and cRGD **(J-R)** exhibit dose-dependent decrease in their ability to form central aggregations of Alexa Fluor 647-labeled ephrin-A1 at cell/bilayer planar interface. **(A, J)** Mean radial density profiles of ephrin-A1-647 under ROCK-drugged cells as measured by epifluorescence microscopy. Trial sample sizes range from 29 to 41 cells. Error bars represent standard error of the mean. Bar graph **(J,** *inset***)** represents average integrated ephrin-A1-647 densities observed under ROCK-inhibited cells after 1 hour stimulation on bilayers functionalized with 1:10 cRGD:ephrin-A1-647. **(B-E, K-N)** Epifluorescence images of ephrin-A1-647 densities at cell/bilayer contact interface. **(F-I, O-R)** RICM images showing regions of close cell/bilayer contact. Scale bars: 10μm. Ephrin bilayer data set: four-dose trial with average n=3 cells. RGD-ephrin data set: four-dose trial with average n= 95 cells.

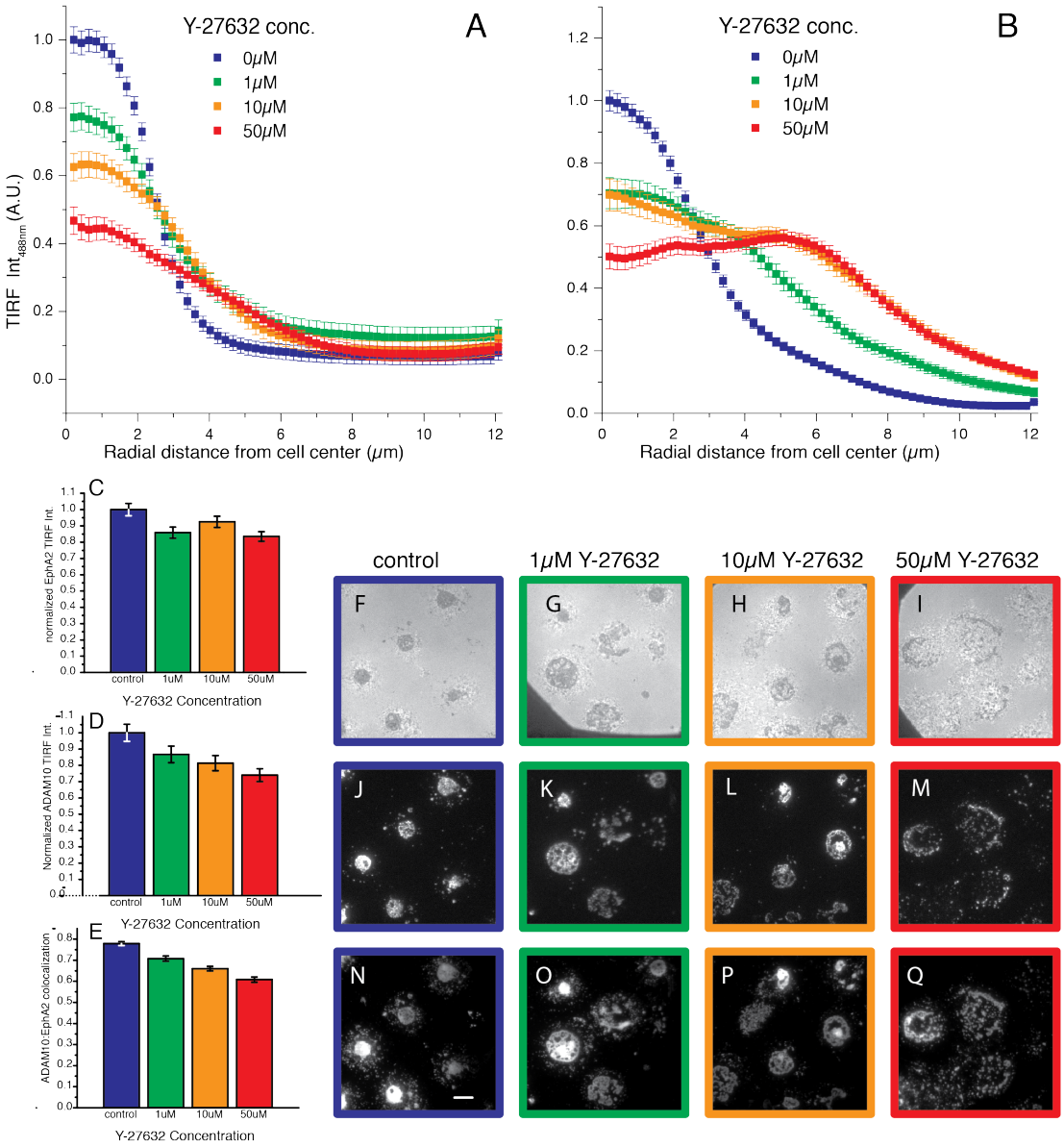

Figure 6. *Biochemical ROCK inhibition progressively disrupts centripetal localization of perimembrane EphA2 and ADAM10.* ROCK-drugged cells cultured for one hour on ephrin-A1-functionalized bilayers and stained for EphA2 and ADAM10 exhibit dose-dependent decreases in the degree of central protein aggregation observed at the planar cell/bilayer planar interface. Mean radial density profiles of **(A)** ADAM10 and **(B)** EphA2 as measured by TIRF microscopy readouts of antibody label intensity. Error bars represent standard error of the mean. Although ROCK inhibition had relatively little effect on the density of

EphA2 observed at the cell/bilayer interface as measured by TIRF intensity of antibody signal after staining **(C),** ROCK inhibition progressively decreased both the amount of ADAM10 observed at the cell/bilayer interface consequent to stimulation with bilayer ephrin-A1 **(D)** and the degree of interfacial colocalization observed between ADAM10 and EphA2**(E).** Images are RICM **(F-I),** EphA2 647 stain **(J-M),** and ADAM10 488 stain **(N-Q).** Scale bar: 10μm. Data set analyzed represents 5 four-dose trials with average n=127 cells.

Chapter 2

T cell triggering thresholds are modulated by the number of antigen within individual T cell receptor clusters

Work contribution for the investigations detailed in this chapter is as follows: T cell harvest and culture, bilayer fluorescence microscopy and data analysis were performed by Boryana Manz. Grid microfabrication was performed by Rebecca Petit.

This chapter contains text that was originally published in the Journal of Cell Science 108 (Part 3), 2012.

Abstract

T cells react to extremely small numbers of activating agonist peptides. Spatial organization of T cell receptors (TCR) and their peptide-major histocompatibility complex (pMHC) ligands into microclusters is correlated with T cell activation. Here, we have designed an experimental strategy that enables control over the number of agonist peptides per TCR cluster, without altering the total number engaged by the cell. Supported membranes, partitioned with grids of barriers to lateral mobility, provide an effective way of limiting the total number of pMHC ligands that may be assembled within a single TCR cluster. Observations directly reveal that restriction of pMHC content within individual TCR clusters can decrease T cell sensitivity for triggering initial calcium flux at fixed total pMHC density. Further analysis suggests that triggering thresholds are determined by the number of activating ligands available to individual TCR clusters, not by the total number encountered by the cell. Results from a series of experiments in which the overall agonist density and the maximum number of agonist per TCR cluster are independently varied in primary T cells indicate that the most probable minimal triggering unit for calcium signaling is at least four pMHC in a single cluster for this system. This threshold is unchanged by inclusion of coagonist pMHC, but costimulation of CD28 by CD80 can modulate the threshold lower.

Introduction

T cells exhibit an exquisite ability to recognize extremely low densities of agonist peptide antigen displayed in MHC proteins on the surface of antigen-presenting cells. Some studies have suggested that T cells may react to even a few individual agonist peptide molecules [1–3]. Moreover, T cells maintain this extreme sensitivity without spontaneous triggering in the absence of agonist, which could lead to autoimmune disorders[4]. Various mechanisms have been proposed for explaining how high sensitivity to agonist can exist while still allowing apparent immunity to stochastic noise. Some explanations include T cell receptor (TCR) monomer triggering by co-receptor or self-peptide major histocompatibility complex (pMHC) heterodimerization[5, 6] or force-induced conformational changes[7]. Cooperativity among multiple receptors within the TCR-pMHC clusters is also implicated[8], which may result from conformation-induced clustering[9], kinetic segregation[10], or lipid-mediated assembly[11]. However, the specific physical mechanisms by which these remarkable capabilities are achieved remain unresolved, due largely to experimental limitations. Key to ultimately determining and experimentally verifying the molecular mechanism of TCR triggering is the ability to manipulate TCR cluster assembly in living T cells.

In the following, we present results from experiments that directly probe the consequences of differentially partitioning agonist, coagonist, and null pMHC among TCR clusters in primary T cells. The strategy is based on the hybrid live cell–supported membrane configuration, in which a solid supported lipid bilayer takes the place of the antigen presenting cell[12–14] (**Figure 1**). Histidine-tagged variants of MHC class II intercellular adhesion molecule-1 (ICAM-1) and CD80 for costimulation experiments are linked to the membrane through Ni^{2+}-chelating lipid groups[14, 15]. The lipids and proteins diffuse freely and as monomers on the supported membrane[16]. Peptide composition and pMHC density are under direct experimental control. TCR clustering is controlled through grid patterns of metal lines, which have been prefabricated onto the underlying solid substrate. These structures function as lateral mobility barriers[12, 16], frustrating the transport of lipids and supported membrane-associated proteins across the planar surface of the substrate. Molecules diffuse freely within each grid corral, but are unable to hop between separate corrals. As the TCR engage antigen pMHC at high antigen densities, clustering ensues until all pMHC within a single corral of the grid-partitioned supported membrane are coalesced into a single cluster, which colocalizes with a similar cluster of cognate TCR on the anterior surface of the cell[12] (**Figure 1D**). The number of pMHC within each supported membrane corral constitutes the upper limit for the pMHC content of the corresponding TCR clusters that may assemble on the T cell's membrane. By placing onto each substrate grids that exhibit a range of different line spacings, it is possible to "titrate" the maximum number of pMHC bound per TCR cluster without changing the total number of antigens engaged by the T cell. Since the mobilities of the proteins on the surface of the cell are restricted only to the extent that they are linked to substrate-bound ligands, the

total number of TCR and other signaling molecules within clusters is not limited by the substrate partitions. We refer to this physical manipulation of molecular organization within living cells as a *spatial mutation*[12, 17, 18]. In the present application, T cells differing only in the peptide agonist distribution among TCR clusters are generated and compared side-by-side.

The primary goal of the present study is to determine how agonist distribution among TCR clusters governs T cell activation. We perform a two-parameter titration experiment in which the overall antigen peptide surface density as well as its partitioning among TCR clusters are independently controlled in living T cells. The results indicate that the threshold antigen densities for triggering Ca^{2+} flux (in terms of the number of antigens per cell) are dependent on the degree of agonist partitioning among TCR clusters. Most significantly, when antigen dose-response functions obtained on different grid partition sizes are analyzed in terms of the maximum number of antigens per TCR cluster (determined by pMHC content within individual membrane corrals), they collapse onto a single curve.

We observe that T cells trigger at an average agonist density of approximately two per TCR cluster, irrespective of the total number of agonist engaged by the cell. The term "triggering threshold" is used here to describe the average density at which half-maximum response is achieved. Observed triggering thresholds were not changed by inclusion of the coagonist null peptide ER60. Interpretation of this invariant activation response in terms of the Poisson distribution of agonist pMHC among TCR clusters indicates that the most likely activation threshold is at least four agonist peptides within a single TCR cluster in this system. However, since T cells do not have a universal threshold for triggering, this implies only that when T cell stimulation is allowed to proceed under a stringently-controlled set of specific conditions, numerical activating thresholds are reproducibly observed. One example of the variables under experimental control is the inclusion of CD80 in the supported membrane, which activates the costimulatory receptor CD28 on the T cells, lowering triggering thresholds. The implications of these measurements with respect to the mechanism of TCR signaling are discussed.

Results and Discussion

Physical Partitioning of T cell Receptor Clusters

T cell activation is investigated in a hybrid immunological synapse consisting of primary mouse T cells interacting with functionalized supported lipid bilayer membranes (**Figure 1A**). This configuration is widely used and has been instrumental in characterizing the immunological synapse[8, 12, 13]. Glass substrates organize spontaneous self-assembly of supported membranes from small unilamellar vesicles. A critical characteristic feature of supported membranes is the free lateral mobility of lipids and membrane-associated proteins[12]. For hybrid immunological synapse reconstitution, the supported membrane is

functionalized with ICAM-1 and MHC loaded with various combinations of agonist [moth cytochrome c (MCC)], null (T102E), and coagonist null (ER60) peptides[8, 12, 13]. For CD28 costimulation studies, CD80 is included in the supported membrane as well. The cytoplasmic domains of these proteins are expressed as histidine-tagged constructs (His10 for ICAM-1 and CD80 and 2XHis6 for MHC) and stably linked to the supported membrane by multivalent interactions with Ni^{2+}-chelating lipids mixed in with the membrane. We employ kinetic control parameters to achieve desired densities of bound protein[14, 15].

AND TCR effector T cells form hybrid junctions with these supported membranes irrespective of the peptide displayed by the MHC, due to the presence of ICAM-1. When all of the MHC is loaded with the null T102E peptide, T cells spread on the surface and exhibit a relatively homogeneous distribution of TCR (**Figure 1B**). At low concentrations of MCC–MHC, TCR organize into clusters throughout the contact zone. At much higher MCC–MHC, these TCR clusters are actively driven towards the center of the interface by an actin polymerization-dependent process, forming the classical immunological synapse pattern[8] (**Figure 1B and C**). TCR cluster formation is coincident with and necessary for activation of downstream calcium flux, but TCR clusters can continue to form after activation[8].

Physical structures on the underlying supported membrane substrate can be used to control TCR clustering in the living cell (**Figure 1D**). Barriers to lateral mobility of supported membrane components are created by metal lines (~10nm high, 100nm wide) that are prefabricated onto the glass substrate by electron beam lithography. The gridline barriers trap fixed numbers of pMHC, along with any other supported membrane proteins, within each corral without otherwise interfering with their mobility. As TCR engage these mobile but trapped pMHC, they also become subject to substrate-imposed constraints. Generally, we observe TCR to accumulate into one microcluster within a single corral. Thus, the number of pMHC per corral determines the maximal number of pMHC per TCR cluster, whereas the number of TCR per cluster is not so limited. TCR outnumber MHC in most clusters; this is especially true when the substrate surface exhibits low pMHC densities. We note that this observation does not indicate that individual TCR-pMHC interactions are long-lived or stable[19]; it indicates only that the TCR cluster is stable at high antigen density. Because our experiments restrict the congregation of pMHC, thereby ensuring that no TCR cluster can ever gather more antigen than is contained within a single substrate corral, our observations are independent of the initial extent of multimerization exhibited by resting TCR[20]. When executed properly, this experimental system allows TCR clusters and bilayer proteins to move freely along the barriers, without crossing them or nonspecifically adsorbing to them[21, 22]. Other molecules on the T cell not interacting directly with cognate ligands in the supported bilayer move freely throughout the entire interface. For example, actin and CD45 are both successfully transported within the immunological synapse irrespective of the degree of corral-induced constraint.

Partitioning of Agonists Among TCR Clusters Alters the Threshold Density to Trigger Intracellular Calcium Flux

The experimental ability to independently control pMHC distribution among TCR clusters enables characterization of TCR cluster signaling with unprecedented specificity. A typical experiment is depicted in **Figure 2.** A population of T cells is allowed to interact with a supported membrane that is partitioned by substrate patterns in one region and unpatterned elsewhere. T cell triggering is monitored via intracellular Ca^{2+} flux using ratiometric fluorescence imaging of fura-2 dye[13, 23] (**Figure2A and B**). Although calcium flux is a quick cellular response[24], population calcium flux is integrated over 20 minutes to include cells responding at different times and provide better signal to noise. The choice of integration time does not alter overall results. The supported membrane is of uniform composition over the entire substrate. Thus, the differences in T cell triggering on and off patterned regions result exclusively from differences in TCR-pMHC cluster size. Lymphocyte function-associated antigen 1 and ICAM-1 clustering is not altered, because each corral contains dozens of ICAM-1 molecules. These experiments are performed at overall MHC density of 100 molecules per μm^2 (±5% SD). At these densities, if all the peptides are the MCC agonist, robust intracellular Ca^{2+} flux is observed at all cell grid sizes[12]. By increasing dilution of MCC using T102E, threshold densities for triggering can be identified.

There are several reasons for choosing as our independent variable agonist-to-null peptide-ratio rather than total MHC. Firstly, under physiologic conditions, T cells generally encounter relatively high MHC density and must search for rare agonist peptides. Secondly, molecules are randomly distributed (Poisson) among the supported membrane corrals and the standard deviation of these distributions is $\sqrt{N}$, where N is the average number of molecules per corral. A more uniform MHC distribution is thus achieved at higher MHC densities. Specific effects of the stochastic distribution of dilute MCC agonist peptide must still be considered for interpretation of TCR signaling, as discussed further below. Thirdly, at high MHC density, typical dilutions of agonist to null of approximately 50–100-fold ensure that, in the rare events of aggregation of homogeneous MHC, the probability of interaction events between multiple agonist-loaded MHCs is minimal.

Quantitative results from a representative TCR cluster agonist titration experiment are illustrated in **Figure 2B and C**. This experiment is performed with an overall MCC–MHC density of 8.6 μm^{-2}. At this density, similarly high rates of cell-triggering were observed both off grid and on 1-μm grids (**Figure 2B**). The intrinsic heterogeneity of the T cells, even in TCR transgenic populations, underlies the range of responses—from high to no calcium flux—displayed in the population heat maps[25]. 0.5-μm grid partitioning, by contrast, effectively blocked activation. Population responses are further compared by the average integrated calcium response over 20 minutes, which reports on early TCR signaling[2] (**Figure 2C**). Note that the barrier line width is not negligible and must be accurately

measured by scanning electron microscopy and quantitative fluorescence to calculate the correct membrane area in different grid sizes. Control patterns consist of arrays of solid squares with chrome area coverage levels similar to those of the grids. These squares, which do not restrict MHC mobility or partition TCR clusters, yield activation ratios similar to those observed off-grid. This control experiment provides critical confirmation that the presence of metal on the substrate does not appreciably alter T cell response.

When TCR clusters were finely partitioned on the 0.5-μm grids, triggering was essentially prevented without changing the total number of agonist pMHC engaged by the cell. Thus, the minimum agonist density recognized by T cells depends on how agonists are distributed among TCR clusters. From this observation, we may also conclude that, at the very least, a single agonist pMHC per TCR cluster is insufficient to trigger Ca^{2+} flux.

Minimal Number of Agonist Per Signaling TCR Cluster

What *is* the minimum number of agonist pMHC per TCR cluster sufficient for triggering Ca^{2+} flux? We explore this question through a series of experiments in which agonist pMHC density is titrated off and on two different grid sizes, 1 and 0.5 μm. As seen in **Figure 3A**, as grid size and TCR-pMHC cluster size get smaller, the activation density necessary for triggering Ca^{2+} flux becomes progressively higher. At sufficiently high concentration of MCC–MHC, cells can activate on both grid sizes. If these independent titration curves are instead plotted in terms of the number of agonist pMHC per cluster, then the 1- and 0.5-μm activation curves collapse to a single dose-response function (**Figure 3B**). At an average of one MCC–MHC per box, T cells remain inactive; at two, they become active. This result is obtained irrespective of the total number of agonist pMHC engaged by the cell or the dimensions of the grid box. The fact that there are four times as many TCR clusters in the more finely-partitioned 0.5-μm grid cells does not affect this threshold. Additional increases in triggering Ca^{2+} flux as agonist pMHC density increases further are much more gradual. The onset of triggering abruptly occurs once a critical number of agonist pMHC per TCR cluster is reached. This fundamental observation has been repeated no less than nine times with populations of T cells from at least four different mice and observed with GPI-tethered proteins as well (**Figure 6**).

At such low densities, the stochastic distribution of agonist pMHC among the many TCR clusters in each cell must be considered. In our experimental procedure, both agonist and null peptide loaded MHC are exposed to the membrane from solution simultaneously[26]. We can therefore expect uncorrelated binding of both peptide–MHC complexes. The peptide off rate is extremely slow and peptide reloading from solution is negligible at neutral pH[27]. Thus the original loading configuration is expected to persist throughout the entire experiment, which results in a Poisson distribution for the number of agonist MCC peptides in each grid box. The probability of a given TCR cluster having a particular number of agonist pMHC for different average numbers of agonist pMHC per cluster is plotted in **Figure 3C**.

Next, we compare the distribution of agonist among TCR clusters at an average MCC–MHC density of one per cluster, which was not activating, to an MCC–MHC density of two per cluster, which *was* activating, as traced by gray lines between **Figure 3B and C**. Notice that the probability of two MCC–MHC in a single cluster is relatively unchanged and the probability of two or more MCC-MHCs changes by less than twofold between the non-activating and activating situations. In contrast, the number of TCR clusters with three and, to an even greater extent, four or more MCC–MHCs has risen sharply (**Figure 3D**). These results indicate that the most probable minimal triggering unit contains at least four agonist pMHC in a single TCR cluster and could require as many as six. Because of the low probability of the congregation of more than six agonists in any single TCR cluster, it is unlikely that numbers this high are required.

In the experiments described above, agonist MCC peptide was titrated into a majority background of the null peptide, T102E. There is another group of endogenous peptides, referred to as coagonists, which do not activate by themselves at any density, preferring instead to enhance activation in the presence of agonist pMHC[5, 28]. A peptide from the cysteine protease of the endoplasmic reticulum (ER60) has been reported as a coagonist peptide to effector T cells, bearing the 5C.C7 TCR receptor that also recognizes MCC–MHC[5]. MCC titration experiments were also performed by dilution into a background of ER60 (**Figure 4**). Triggering thresholds with ER60 are the same as measured for MCC titrations into the absolute null T102E, and exhibit the same universality on a per TCR cluster basis. However, ER60 did yield an apparent increase in the magnitude of Ca^{2+} flux.

The costimulatory molecule CD80 can also modulate T cell signaling by activating CD28 on the T cell surface[29, 30]. Inclusion of CD80 (approximately 300 molecules per μm^2)[14] in the supported membrane during MCC:T102E titration experiments yields two distinct effects on TCR signaling (**Figure 5A**). Firstly, the triggering threshold is notably shifted to lower agonist pMHC densities. Additionally, the apparent magnitude of Ca^{2+} flux was shown to increase in a manner similar to that observed with the coagonist ER60 peptide. This stronger activation with CD80–CD28 costimulation is in agreement with the results of previous investigations[29].

Renormalization of the MCC:T102E titration responses from both grid sizes in terms of the number of antigen per grid box again yields a singular response curve (**Figure 5B**). Although we observe that triggering thresholds are shifted by CD80–CD28 costimulation, they are still best defined on a per TCR cluster basis, rather than a per cell basis. A stochastic analysis of agonist distribution among clusters as done above reveals the most probable minimum activating unit in the presence of CD80–CD28 costimulation is two agonist pMHC per TCR cluster (**Figure 5C and D**). The data is a bit rougher at these very low triggering thresholds, but it is important to realize that if a single agonist peptide could cause a TCR cluster to trigger, then there would be no partition effect. The data presented here are thus not consistent with an individual agonist activating a TCR cluster.

The difference between the measured triggering threshold based on average and stochastic analyses deserves consideration. We first note that triggering, as defined by rising intracellular Ca^{2+}, is essentially binary, since the onset of Ca^{2+} flux is abrupt. The next question, then, concerns whether individual TCR clusters trigger with an all-or-nothing or a graded response. Based on the experimental evidence reported here, it is unlikely TCR clusters could yield a graded response at minimal antigen levels. We arrive at this conclusion based on the fact that partitioning TCR clusters at a constant total amount of antigen leads to an abrupt cessation of triggering. If multiple partially-triggered TCR clusters were somehow integrated within the cell to yield the equivalent of one fully-triggered cluster, then such discrete changes as a function of partitioning alone are not expected.

These results are most consistent with a mechanism in which individual TCR clusters trigger on a binary (all or nothing) basis after achieving some minimum threshold. Such a response necessitates extensive cooperativity among the TCRs within individual clusters[31]. It is possible that more TCRs are triggered than the number of agonists within individual clusters, at least to the extent that triggering of an individual TCR can be defined[3]. The serial triggering model[3, 32] provides one mechanism for such a phenomenon. There are also reports suggesting some degree of TCR preclustering[20], which would provide a mechanism for recruiting and possibly triggering TCR not directly engaged with antigen pMHC. With this all-or-nothing response, the probability of a TCR cluster triggering will be a function of the number of agonists in the cluster. However, it is not necessary that a specific threshold number of agonist per cluster—above which the cluster always triggers and below which it never does—even exist. Rather, all we can expect is that the probability of a cluster triggering increases with agonist number and that this increase may be particularly abrupt around a certain critical number of agonists per cluster. Our experimental results reveal abrupt increases in the probability of triggering intracellular Ca^{2+} flux corresponding with the appearance of TCR clusters containing at least four agonist pMHC in the absence of costimulation.

Observation with CD80–CD28 costimulation reveals that TCR triggering thresholds are not absolute. CD80–CD28 costimulation is one of perhaps multiple ways that triggering thresholds may be tuned in vivo[5, 19, 30, 33, 34]. Naïve T cells, which are dependent on this costimulation, may have much higher signaling thresholds. The one truly invariant observation among all of the results presented here is that triggering thresholds are determined on a per TCR cluster basis, and not on a per T cell basis.

Previously, direct coupling of two TCRs by bivalent antibody or agonist dimers has been shown to trigger T cells[5, 35]. These well known facts, along with structural evidence of TCR-binding to CD4[36, 37], naturally lead to the speculation that a TCR dimer may be the fundamental triggering unit. However, the artificial tether between agonists alters the dynamics of agonist–TCR and TCR–TCR association, possibly stabilizing it beyond

physiologic conditions, and therefore cannot reveal the native threshold for triggering. The experimental design used here neither enforces nor requires direct dimerization between agonist pMHCs. Estimates of T cell sensitivity to pMHC have been made with increasing precision over the past two decades because of advances in quantitative measurements of peptide number and characterization of early T cell responses[1, 38–41]. Single agonist sensitivity has been reported by fluorescence in a cell–cell interface where multiple ligands, protein complexes, and coagonist endogenous peptides are present[1, 2, 5]. There are several factors to consider when interpreting these reports in light of the results we present here. First, our definition of triggering threshold as the average antigen number at which half-maximum response is achieved may differ from earlier interpretations. We chose this definition because it converges to an informative value in the limit of a large number of experiments. Triggering threshold cannot properly be defined as the lowest level of antigen at which any triggering was observed, because there is a nonzero probability of a cell triggering with no antigen due to stochastic fluctuations; this stochastic triggering cannot be distinguished from causal triggering on a cell-by-cell basis. Secondly, supported membranes differ from live antigen presenting cell (APC) experiments because costimulatory molecule and peptide antigen distributions are directly controllable. These are intrinsically unknown in live APCs, and may alter triggering thresholds[5, 42]. Although the supported membrane system may be less physiologic than live APCs, it is far better controlled and therefore offers more quantitative information on the behavior of the TCR signaling system under specific conditions.

In conclusion, the TCR cluster size titration experiments described here arguably constitute the most quantitative analysis of TCR triggering thresholds to date. The results are generally consistent with the extreme, near-single-molecule sensitivity of T cells to antigen long thought to exist. Cluster size titration further reveals that spatial organization into TCR clusters is critical to achieve this sensitivity. The universal observation that Ca^{2+} flux triggering thresholds were determined on a per TCR cluster basis, rather than a per T cell basis, raises interesting questions concerning large-scale cooperativity in receptor signaling clusters and apparent lack of cooperativity between clusters.

Materials and Methods

Mice and T cells

AND CD4+ T cell blasts were prepared by in vitro stimulation of spleen and lymph node cells from an F1 cross of ANDxB10. BR mice (Jackson Laboratory) with 1–2 μM MCC peptide. Cells were maintained in IL-2 every 48 hours and used on days 5 and 7.

Patterned Supported Proteolipid Bilayers

Glass slides were patterned by e-beam lithography at University of California, Berkeley Microfabrication Lab and Molecular Foundry, Lawrence Berkeley National

Laboratory. Liposomes with 97.5 mol % 1,2-dioleoyl-sn-glycero-3-phosphocholine, 2 mol % 1,2-dioleoyl-sn-glycero-3-[(N-(5-amino-1-carboxypentyl)iminodiaceticacid)succinyl] (nickel salt) and 0.5 mol% Texas Red® 1,2-dihexadecanoylsn-glycero-3-phosphoethanolamine, triethylammonium salt, prepared by sonication or extrusion, were injected over substrate in a Biophtech FCS2 flow chamber. His-tagged proteins were expressed in Hi5 cells and purified by Ni-nitrilotriacetic acid affinity[14, 22]. Surface density of MCC–MHC was measured with Alexa Fluor conjugated MCC peptide and calibrated with supported bilayers[43].

Fluorescence Imaging.

For calcium flux, cells were loaded with 1 μM fura-2-acetoxymethyl and imaged at 340 and 380 nm with emission at 510 nm via 40xS Fluor objective on Quantix 57 or CoolSnap K4 cameras. Fields of view with patterns were monitored every 7 or 15 s for 20 min. Cell motion and fluorescence intensity were tracked and analyzed semi-automatically in Imaris, Metamorph, Matlab, and Excel. TCR, actin, and CD45 were imaged via 100x N.A. 1.3 objective on a CoolSnapHQ camera. Total internal reflection fluorescence (TIRF) was done via 100x N.A. 1.45 TIRF objective on a Cascade 512B EM CCD camera.

Chapter 2 References

1. Sykulev ,Y., Joo, M., Vturina, I., Tsomides, T.J., Eisen, H.N. Evidence that a single peptide-MHC complex on a target cell can elicit a cytolytic T cell response. *Immunity* **4**, 565–571 (1996).

2. Irvine, D.J., Purbhoo, M.A., Krogsgaard, M., Davis, M.M. Direct observation of ligand recognition by T cells. *Nature* **419**, 845–849 (2002).

3. Stefanova, I., Dorfman, J.R., Germain, R.N. Self-recognition promotes the foreign antigen sensitivity of naive T lymphocytes. *Nature* **420**, 429–434 (2002).

4. Wylie, D.C., Das, J., Chakraborty, A.K. Sensitivity of T cells to antigen and antagonism emerges from differential regulation of the same molecular signaling module. *Proc. Natl. Acad. Sci. USA* **104**, 5533–5538 (2007).

5. Krogsgaard, M., et al. Agonist/endogenous peptide-MHC heterodimers drive T cell activation and sensitivity. *Nature* **434**, 238–243 (2005).

6. Trautmann, A., Randriamampita, C. Initiation of TCR signaling revisited. *Trends Immunol.* **24**, 425–428 (2003).

7. Li, Y.C., et al. Cutting edge: Mechanical forces acting on T cells immobilized via the TCR complex can trigger TCR signaling. *J. Immunol.***184**, 5959–5963 (2010).

8. Varma, R., Campi, G., Yokosuka, T., Saito, T., Dustin, M.L. T cell receptor-proximal signals are sustained in peripheral microclusters and terminated in the central supramolecular activation cluster. *Immunity* **25**, 117–127 (2006).

9. Lillemeier, B.F., et al. TCR and Lat are expressed on separate protein islands on T cell membranes and concatenate during activation. *Nat. Immunol.* **11**, 90–96 (2010).

10. Davis, S.J., van der Merwe, P.A. The kinetic-segregation model: TCR triggering and beyond. *Nat. Immunol.* **7**, 803–809 (2006).

11. Horejsi,V. Lipid rafts and their roles in T cell activation. *Microbes Infect.* **7**, 310–316 (2005).

12. Mossman, K.D., Campi, G., Groves, J.T., Dustin, M.L. Altered TCR signaling from geometrically repatterned immunological synapses. *Science* **310**, 1191–1193 (2005).

13. Grakoui, A., et al. The immunological synapse: A molecular machine controlling T cell activation. *Science* **285**, 221–227 (1999).

14. Nye, J.A., Groves, J.T. Kinetic control of histidine-tagged protein surface density on supported lipid bilayers. *Langmuir* **24**, 4145–4149 (2008).

15. Groves, J.T., Dustin, M.L. Supported planar bilayers in studies on immune cell adhesion and communication. *J. Immunol. Methods* **278**, 19–32 (2003).

16. Groves, J.T, Ulman, N., Boxer, S.G. Micropatterning fluid lipid bilayers on solid supports. *Science* **275**, 651–653 (1997).

17. Groves, J.T. Spatial mutation of the Tcell immunological synapse. *Curr. Opin. Chem. Biol.* **10**, 544–550 (2006).

18. Salaita, K., et al. Restriction of receptor movement alters cellular response: physical force sensing by EphA. *Science* **327**, 1380–1385 (2010).

19. Huppa, J.B., et al. TCR-peptide-MHC interactions in situ show accelerated kinetics and increased affinity. *Nature* **463**, 963–967 (2010).

20. Alarcon B, Swamy M, van Santen HM, Schamel WW. T cell antigen-receptor stoichiometry: Pre-clustering for sensitivity. *EMBO. Rep.* **7**, 490–495 (2006).

21. DeMond, A.L., Mossman, K.D., Starr, T., Dustin, M.L., Groves, J.T. T cell receptor microcluster transport through molecular mazes reveals mechanism of translocation. *Biophys. J.* **94**, 3286–3292 (2008).

22. Hartman, N.C., Nye, J.A., Groves, J.T. Cluster size regulates protein sorting in the immunological synapse. *Proc. Natl. Acad. Sci. USA* **106**, 12729–12734 (2009).

23. Wulfing, C., et al. Kinetics and extent of T cell activation as measured with thecalcium signal. *J. Exp. Med.***185**, 1815–1825 (1997).

24. Huse, M., et al. Spatial and temporal dynamics of T cell receptor signaling with a photoactivatable agonist. *Immunity* **27**, 76–88 (2007).

25. Feinerman, O., Veiga, J., Dorfman, J.R., Germain, R.N., Altan-Bonnet, G. Variability and robustness in T cell activation from regulated heterogeneity in protein levels. *Science* **321**, 1081–1084 (2008).

26. Reay, P.A., Kantor, R.M., Davis, M.M. Use of global amino acid replacements to define the requirements for MHC binding and T cell recognition of moth cytochrome c (93–103). *J. Immunol.* **152**, 3946–3957 (1994).

27. Boniface, J.J., et al. pH affects both the mechanism and the specificity of peptide binding to a class II major histocompatibility complex molecule. *Biochemistry* **32**, 11761–11768 (1993).

28. Ebert, P.J., Jiang, S., Xie, J., Li, Q.J., Davis, M.M. An endogenous positively selecting peptide enhances mature T cell responses and becomes an autoantigen in the absence of microRNA miR-181a. *Nat. Immunol.* **10**, 1162–1169 (2009).

29. Andres, P.G., et al. CD28 signals in the immature immunological synapse. *J. Immunol.* **172**, 5880–5886 (2004).

30. Yokosuka, T., et al. Spatiotemporal regulation of T cell costimulation by TCRCD28 microclusters and protein kinase C theta translocation. *Immunity* **29**, 589–601 (2008).

31. Martinez-Martin N, et al. Cooperativity between T cell receptor complexes revealed by conformational mutants of CD3epsilon. *Sci. Signal.* **2**(83), p. ra43 1–11 (2009).

32. Valitutti, S., Muller, S., Cella, M., Padovan, E., Lanzavecchia, A. Serial triggering of many T cell receptors by a few peptide-MHC complexes. *Nature* **375**, 148–151 (1995).

33. Huang, J., et al. The kinetics of two-dimensional TCR and pMHC interactions determine T cell responsiveness. *Nature* **464**, 932–936 (2010).

34. Henrickson, S.E., et al. Cell sensing of antigen dose governs interactive behavior with dendritic cells and sets a threshold for T cell activation. *Nat. Immunol.* **9**, 282–291 (2008).

35. Cochran, J.R., Cameron, T.O., Stern, L.J. The relationship of MHC-peptide binding and T cell activation probed using chemically defined MHC class II oligomers. *Immunity* **12**, 241–250 (2000).

36. Li, Q.J., et al. CD4 enhances T cell sensitivity to antigen by coordinating Lck accumulation at the immunological synapse. *Nat. Immunol.* **5**, 791–799 (2004).

37. Wang, J.H., et al. Crystal structure of the human CD4 N-terminal two-domain fragment complexed to a class II MHC molecule. *Proc. Natl. Acad. Sci. USA* **98**, 10799–10804 (2001).

38. Harding, C.V., Unanue, E.R. Quantitation of antigen-presenting cell MHC class-II peptide complexes necessary for T cell stimulation. *Nature* **346**, 574–576 (1990).

39. Demotz, S., Grey H.M., Sette, A. The minimal number of class-II MHC antigen complexes needed for T cell activation. *Science* **249**, 1028–1030 (1990).

40. Kimachi, K., Croft, M., Grey, H.M. The minimal number of antigen-major histocompatibility complex class II complexes required for activation of naive and primed T cells. *Eur. J. Immunol .* **27**, 3310–3317 (1997).

41. Reay, P.A., et al. Determination of the relationship between T cell responsiveness and the number of MHC-peptide complexes using specific monoclonal antibodies. *J. Immunol.* **164**, 5626–5634 (2000).

42. Anderson, H.A., Hiltbold, E.M., Roche,P.A. Concentration of MHC class II molecules in lipid rafts facilitates antigen presentation. *Nat. Immunol.* **1**, 156–162 (2000).

43. Galush, W.J., Nye, J.A., Groves, J.T. Quantitative fluorescence microscopy using supported lipid bilayer standards. *Biophys. J.* **95**, 2512–2519 (2008).

Chapter 2 Figures

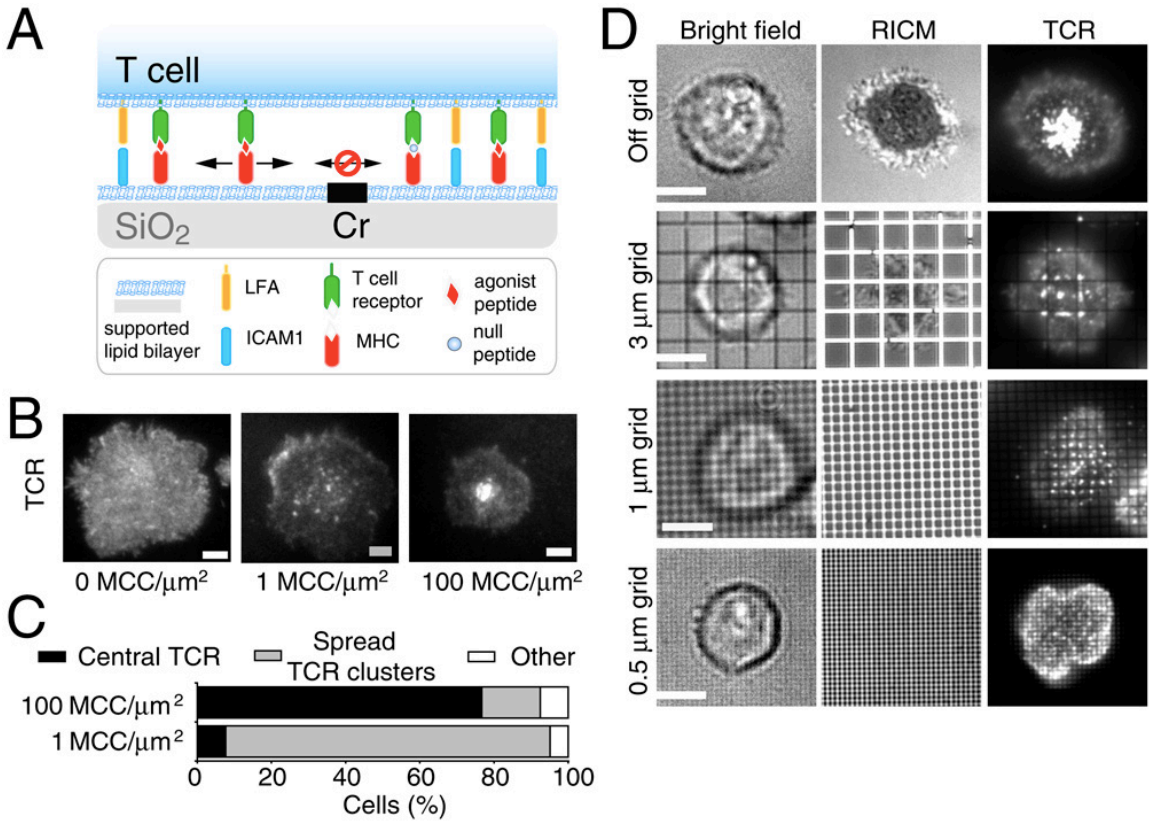

Figure 1. *Immunological synapse on partition patterns.* **(A)** Schematic of experimental strategy. Primary mouse T cells interact with MHC and ICAM-1-functionalized, patterned and supported lipid bilayer membrane. MHC density is constant. MHC is preloaded with an appropriate ratio of null (T102E) and agonist (MCC) peptide. Chromium lines prefabricated on the glass are diffusion barriers to all lipids and lipid-tethered proteins. **(B)** *En face* view of TCR distribution in the immunological synapse. TIRF images of anti-TCR Fab on 0 MCC–MHC μm^{-2} 1 min after contact (diffuse TCR), 1 MCC–MHC μm^{-2} 10 min after contact (small spread TCR clusters), and 100 MCC–MHC μm^{-2} 10 min after contact (large central TCR cluster). Image intensity is scaled to demonstrate clearly the TCR distribution in each case. *(Scale bar: 5 µm.)*
(C) Percent of cells with the TCR distribution phenotypes in B. Ten minutes after contact with bilayer from a representative experiment; n=140–150 cells per concentration. Cells with both a large central cluster and peripheral small clusters are scored in the central large cluster category, because some

TCR transport to the center has occurred. **(D)** Bright field, reflection interference contrast microscopy (RICM), and TCR distribution of cells off grid, and on 3, 1, and 0.5 μm pitch grids after 5–10 min of contact with the surface. TCRs cluster until there is one TCR cluster per box; 100 ±5% SD MCC–MHC μm^{-2}. (*Scale bar: 5 μm.)*

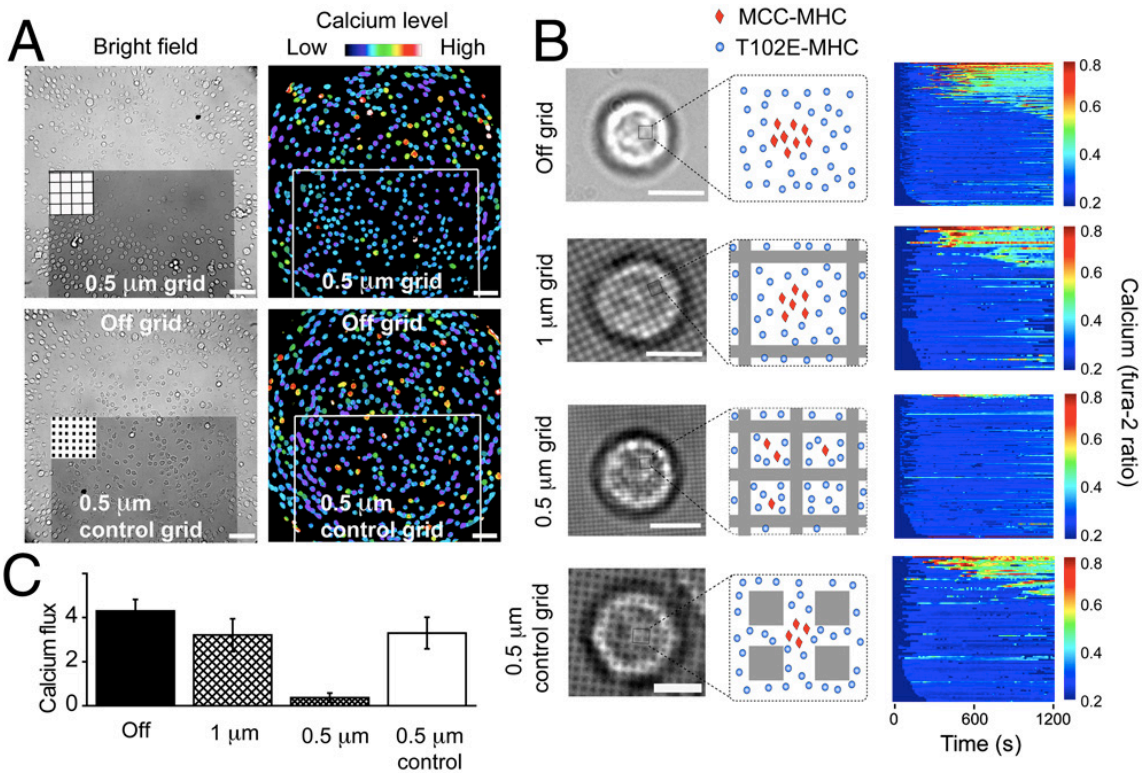

Figure 2. *T cell activation on patterned partition grids.* **(A)** Bright field of T cells and grid *(Left)* and false-colored calcium levels (fura-2 ratio) *(Right). (Upper)* Off and on 0.5-μm square grid. *(Lower)* Off and on 0.5-μm control array of isolated solid squares. Small schematics of patterns are overlaid in bright field image. The white line in the calcium images indicates the border of the grid pattern. Calcium image 8.30 min after cell injection, bright field image approximately 30 minutes after cell injection. (Scale bar: 40 μm.) **(B)** Population calcium flux on partition grids. Bright field of representative cells on and off patterns *(Left),* schematic of possible agonist (MCC) and null (T102E) distribution in grid boxes (Center), and false-colored calcium flux (fura-2 ratio) traces of >100 cells per region *(Right).* (*Scale bar: 5 μm.)* Cell traces (each horizontal line is one cell) are ranked by their integrated calcium flux in descending order. Calcium is imaged every 15 s. **(C)** Population mean (±SEM) of integrated

calcium flux of all cells over 20 min on different size partition grids in A and B. (A–C) All data in this figure are from one representative experiment in one chamber with different patterns spaced approximately 0.3-mm apart; 8.6 ±5% SD MCC–MHC μm^{-2}.

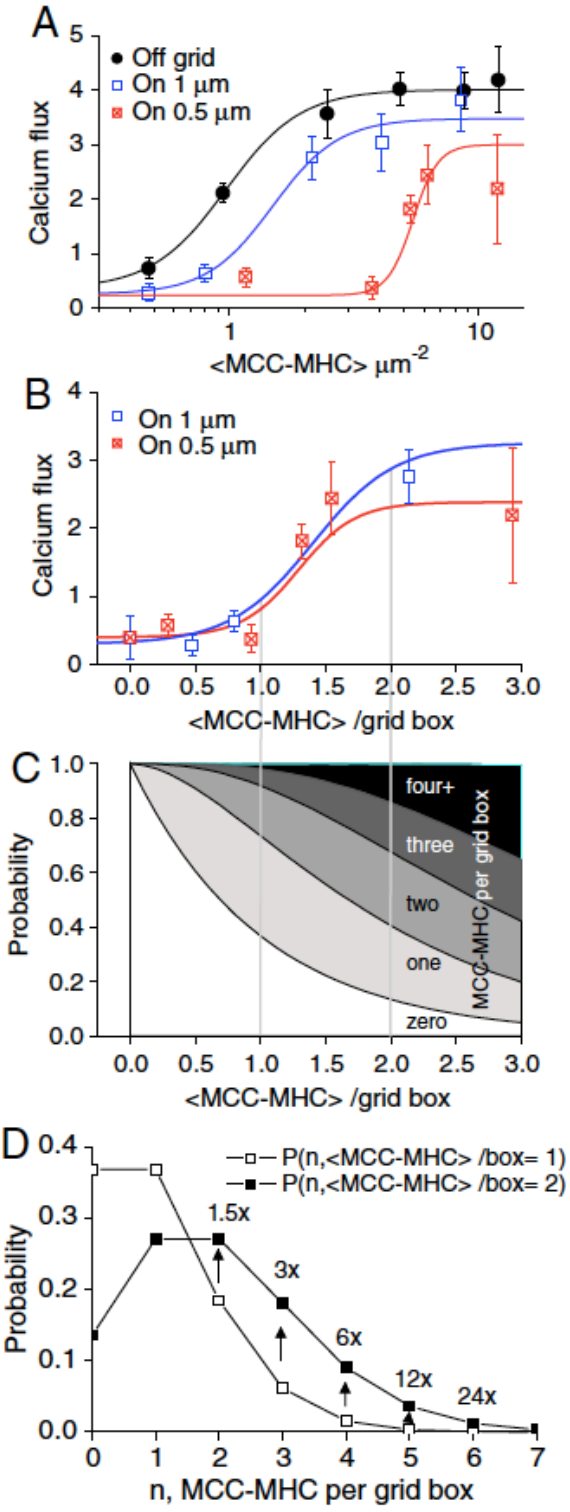

Figure 3. *Partition titration of agonists per TCR cluster.* **(A)** T cell activation with respect to titration of overall MCC–MHC surface density off and on 1- and 0.5-µm partition grids. The minimal density at which T cells activate is shifted higher from off grid (•) to 1-µm grid (□), and even further to 0.5-µm grid (⊠). Lines are guides to the eye. Mean calcium flux (± SEM) of 150–300 cells, pooled from 2–3 independent experiments per concentration. **(B)** T cell activation with respect to number of MCC–MHCs per box at 1-µm (□) and 0.5-µm (⊠) partition grids. The transition to activation on 1- and 0.5-µm grids is at the same number of MCC–MHC per box (between the two gray lines). **(C)** Theoretical Poisson distribution of the probability of discrete number of MCC–MHC per box at different average concentrations per box. At nonactivating density *(left gray line)*, most boxes have zero or one MCC–MHC. At activating densities *(right gray line),* an appreciable number of boxes have more than three or four MCC–MHCs. **(D)** Direct comparison of Poisson probability in C of n (MCC–MHC per grid box) at nonactivating concentration of ⟨MCC-MHC⟩box =1 (□) to activating concentration of 2 (■). Fold increase at each n is marked with an arrow and a numerical value. Probability of n=4–6 goes from negligible to

appreciable and rises sharply between non- and activating concentrations. At activating concentrations, the probability of four agonists is 9%; of 5 is 3.6%; and of 6 is 1.2%, yielding several boxes of each per cell at either grid size (assuming T cell coverage of at

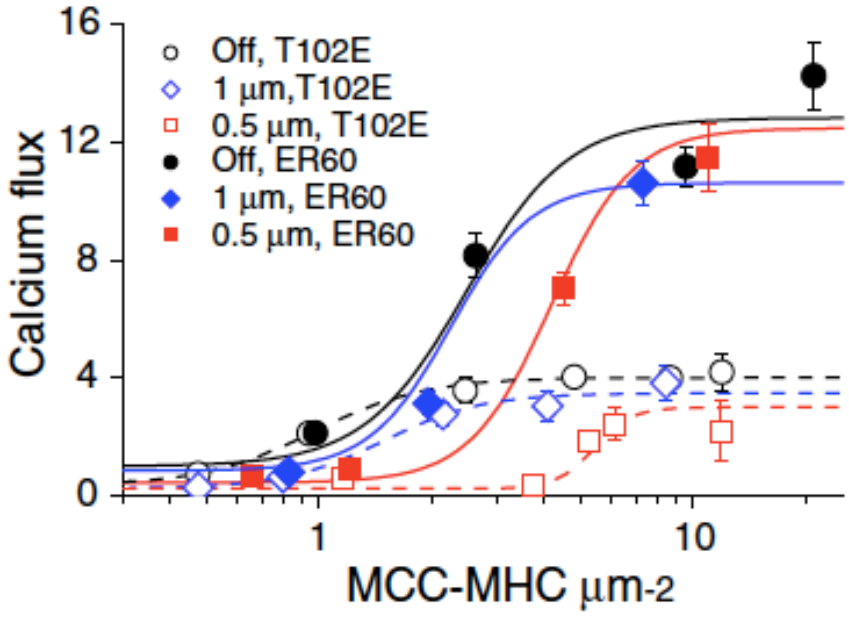

least 100 µm^2).

Figure 4*. Partition titration of agonists per TCR cluster with ER60.* **(A)** Comparison of T cell activation with respect to titration of MCC–MHC surface density off and on 1- and 0.5-µm partition grids, with T102E and ER60 null peptides. The threshold density at which T cells activate off *(circles),* and on 1-µm grid *(diamonds)* (2–3 MCC–MHC µm^{-2}) or 0.5-µm grid *(squares)* (5–6 MCC–MHC µm^{-2}) is the same for background null peptide T102E *(empty symbols)* and ER60 *(filled symbols).* Lines are guides to the eye. Mean calcium flux (± SEM) of more than 80 cells per concentration, from a representative experiment. T102E data are the same as **Figure 3A.**

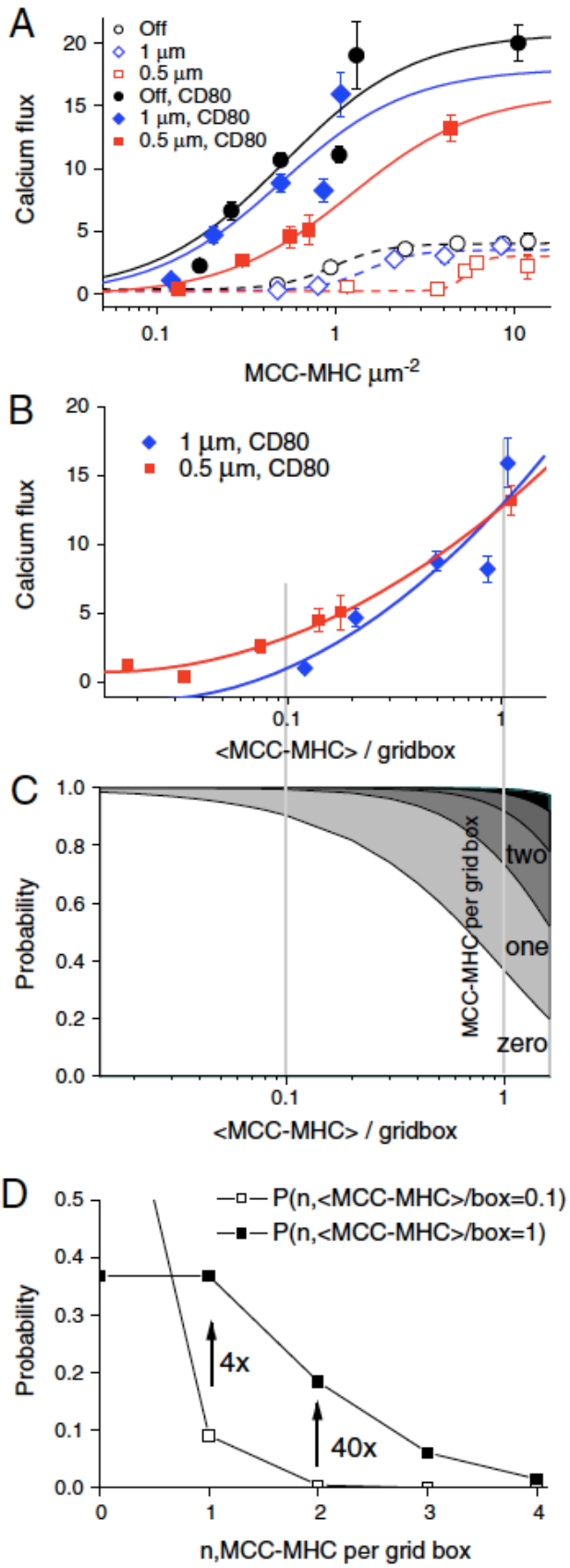

Figure 5. *Partition titration of agonists per TCR cluster with CD80.* **(A)** T cell activation with respect to titration of overall MCC–MHC surface density off and on 1- and 0.5-µm partition grids, with and without CD80. The threshold density at which T cells activate in the presence of CD80 *(filled symbols)* is shifted to the left for cells off grid *(circle),* on 1-µm grid *(diamonds),* and on 0.5-µm grid *(squares).* Lines are guides to the eye. Mean calcium flux (±SEM) of more than 80 cells per concentration, from a representative experiment. Data without CD80 are the same as **Figure 3A.** Null peptide is T102E for all data points. **(B)** T cell activation with respect to number of MCC–MHCs per box at 1-µm *(diamonds)* and 0.5-µm *(squares)* partition grids, in the presence of CD80. The activation profiles for 1- and 0.5-µm grids is the same in terms of number of MCC–MHC per grid box. **(C)** Theoretical Poisson distribution of the probability of discrete number of MCC–MHC per box at different average concentrations per box. At nonactivating density *(left gray line),* most boxes have zero or one MCC–MHC. At activating densities *(right gray line),* an appreciable number of boxes have more than two MCC–MHCs. **(D)** Direct comparison of Poisson probability in *C* of *n* (MCC–MHC per grid box) at nonactivating concentration of⟨MCC-MHC⟩box=0.1 (*open squares)* to activating concentration of 1 *(filled squares)*. Fold increase at each *n* is marked with an arrow and a numerical value. Probability of *n*=2 goes from negligible (0.5%) to appreciable (18%) and rises sharply between non- and activating concentrations in the presence of CD80.

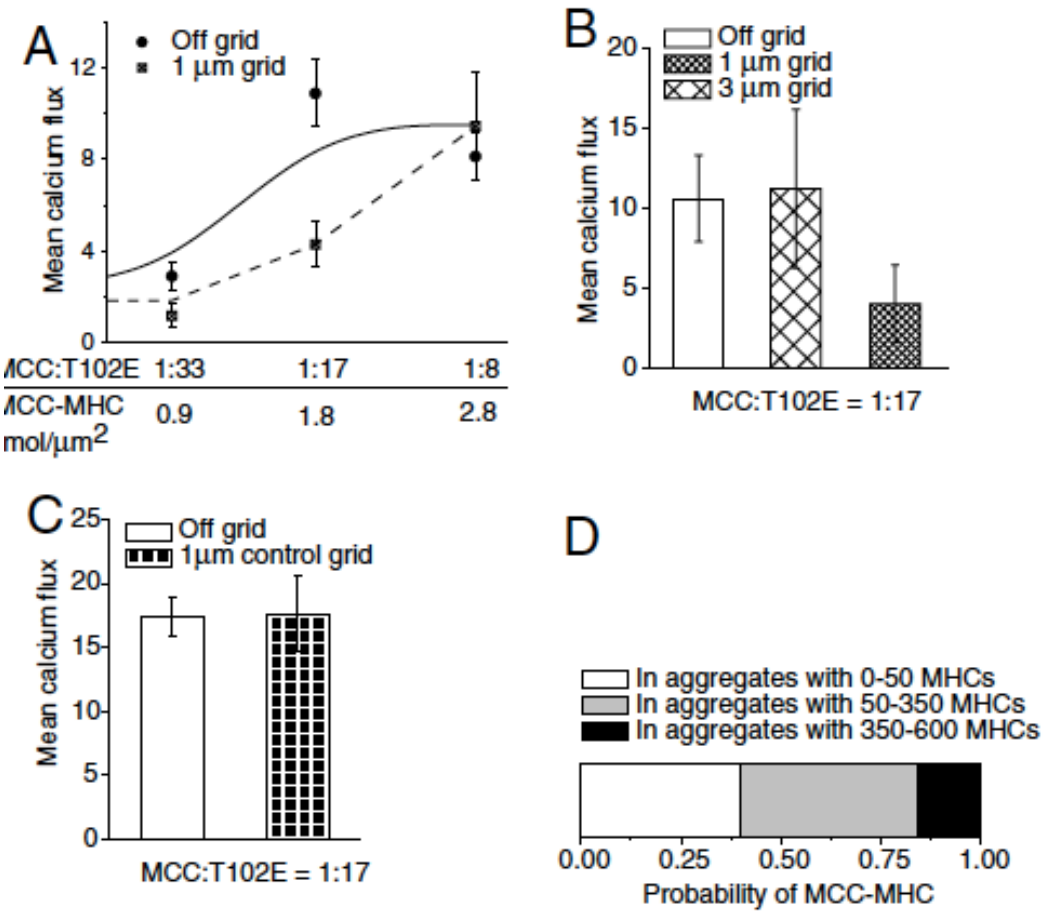

Figure 6. *Titration of MCC–MHC over patterns with GPI-MHC and GPI-ICAM1.* **(A)** Mean calcium flux (±SEM) of T cells from at least three independent experiments. Experimental dilutions and estimated MCC–MHC concentration. Lines are guides to the eye. **(B)** Mean calcium flux (±SEM) of cells from at least three independent experiments off and on 1- and 3-µm grids. **(C)** Mean calcium flux (±SEM) on and off control pattern for 1-µm grid. **(D)** Histogram of MCC distribution in GPI-MCC–MHC aggregates on the supported lipid bilayer.

Chapter 3

Characterization of dynamic actin associations with T-cell receptor microclusters in primary T cells

Work contribution for the investigations detailed in this chapter is as follows: T cell harvest, culture and transduction, bilayer fluorescence microscopy and data analysis were performed by Alex Smoligovets. Grid microfabrication was performed by Rebecca Petit.

This chapter contains text that was originally published in the Journal of Cell Science 125 (Part 3), 2012.

Abstract

T cell triggering through T-cell antigen receptors (TCRs) results in spatial assembly of the receptors on multiple length scales. This assembly is mediated by the T cell actin cytoskeleton, which reorganizes in response to TCR phosphorylation and then induces the coalescence of TCRs into microclusters, followed by their unification into a micrometer-scale structure. The exact outcomes of the association of TCRs with a dynamic and fluctuating actin network across these length scales are not well characterized, but it is clear that weak and transient interactions at the single-molecule level sum to yield significant receptor rearrangements at the plasma membrane. We used the hybrid live cell–nanopatterned supported lipid bilayer system to quantitatively probe the actin–TCR interaction in primary T cells. A specialized tracking algorithm revealed that actin slows as it passes over TCR clusters in a direction-dependent manner with respect to the resistance against TCR motion. We also observed transient actin enrichments at sites corresponding to
putative TCR clusters that far exceeded pure stochastic fluctuations and described an image time-autocorrelation analysis method to quantify these accumulations.

Introduction

T cells are activated when their T-cell antigen receptors (TCRs) are triggered by interactions with antigen peptide–major histocompatibility complex (pMHC) proteins on antigen-presenting cell (APC) surfaces. T cells exhibit exquisite selectivity and sensitivity, and the physical basis for these attributes within the TCR signaling system has attracted much interest. A significant aspect of TCR triggering is the spatial assembly of receptors on multiple length scales. At the scale of the cell itself, TCRs are visibly transported towards the center of the T-cell–APC interface, and the resulting spatial patterns of TCRs and other molecules are called the immunological synapse[1, 2]. Physically interfering with these transport processes can induce detectable changes in T cell signaling, such as phosphorylation of immunoreceptor tyrosine-based activation motifs on the TCR complex and intracellular calcium flux[3]. On shorter time and length scales, TCRs form microclusters upon engagement with pMHC[4–6]. Much of the relevant signaling activity takes place within these TCR microclusters, which function as integrated signaling machines.

Underlying the spatial assembly and transport of TCRs during T cell activation are interactions between the receptors and the actin cytoskeleton[7–9]. In response to TCR triggering, the cytoskeleton transitions from a crawling morphology to a pattern of centripetal flow[10–13]. Simultaneously, TCR microclusters coalesce and translocate towards the center of the immunological synapse. Both coalescence and translocation are actin-dependent, as disruption of the cytoskeleton with latrunculin prevents both processes[14, 15]. Additionally, recent work has shown that actin can affect local TCR–pMHC binding kinetics[16, 17], illustrating another mechanism for involvement of the cytoskeleton in signaling.

TCR microclusters neither need to move at the same speed as the retrograde flowing actin[12, 18], nor do they need to move in the same direction. When translocating microclusters encounter physical obstacles imposed using patterned supported membrane substrates, the microclusters are deflected and move at angles to the actin flow with speeds that exhibit a cosine scaling law, which is consistent with dissipative, or frictional, actin-coupling mechanisms[8]. In other words, numerous weak interactions sum to yield a net force on the TCR microcluster, but there appears to be no stable or elastic association with the actin network. Such frictional coupling mechanisms appear to extend beyond the TCR in the immunological synapse. Differentially clustering the integrin lymphocyte function-associated antigen 1 (LFA-1) using antibodies has been shown to redirect this protein to different positions within the synapse, with the most highly clustered LFA-1 ending up in the center along with TCRs[19].

Although a significant role for actin in the immunological synapse is clear, many physical aspects of actin–TCR interactions are still relegated to the imagination. Preliminary observations of actin engaged in such interactions have been made in Jurkat cells[12, 18], but although these are a tractable T-cell-based model system, they have

important differences from primary T cells[20–22]. Because their TCR agonist is not known, Jurkat cells must be triggered through artificial antibody-induced crosslinking of their CD3 receptors, which inherently supplants endogenous TCR–TCR associations and has the potential to overstabilize the microcluster. This might add to already-documented differences in membrane protein organization between Jurkat cells and primary T cells[20]. Furthermore, a number of Jurkat cell proteins exhibit levels of phosphorylation unlike those of their primary T cell counterparts, including known actin regulatory molecules such as Pyk2 and Vav1[21]. These differences raise questions about findings from studies based on Jurkat cell studies and necessitate the ultimate characterization of actin cytoskeleton behavior in primary cells.

In this study, we quantitatively characterized cortical actin motion within antigen-triggered primary T cells to obtain a deeper level of understanding of the elaborate interactions between the cytoskeleton and the plasma membrane during T cell activation. We employed the hybrid live cell–nanopatterned supported lipid bilayer system, which allows both for assembly of TCR microclusters through interactions with laterally mobile, membrane-tethered pMHC and control of the lateral mobility of these microclusters with nanopatterned barriers in the substrate[3, 23, 24]. Analysis was performed using vector-field identification and tracking algorithms to characterize actin lateral movement and image time-autocorrelation to extract dynamic fluctuations. We observed that the actin cytoskeleton responds to laterally confined TCR clusters by slowing down in their vicinity, a result consistent with a previous report utilizing Jurkat T cells[18], and that the slowing is direction-dependent with respect to the resistance against TCR motion. Image time-autocorrelation revealed that the entire actin assembly forms and disassembles *en masse*. From this observation, we postulate that the primary stability of TCR microclusters originates from the receptors themselves, or other molecules in the microcluster, and that this stability templates assembly of the more dynamic actin, ultimately leading to a linkage to the bulk cytoskeleton.

Results and Discussion

Immunological synapse formation on supported lipid bilayers and nanopatterned substrates

We visualized the cortical actin cytoskeleton in primary murine T cells during immunological synapse formation by allowing primed T cells to interact with a supported lipid bilayer functionalized with pMHC and intercellular adhesion molecule -1 (ICAM-1) proteins (**Figure 1A**). This well-established system simulates the APC surface and effectively triggers T cells while allowing the use of total internal reflection fluorescence (TIRF) microscopy to image events within hundreds of nanometers of the cell–bilayer interface[25–27]. An actin-binding probe composed of enhanced green fluorescent protein (EGFP) bound to the calponin homology domain of utrophin (EGFP–UtrCH) enabled

observation of F-actin dynamics[28], and key observations made with EGFP–UtrCH were validated using EGFP–b-actin.

Experiments in which the spatial configuration of the immunological synapse is physically altered with nanopatterned substrates have proven informative in a variety of studies[24, 25]. Substrates patterned with grids of continuous metal lines (typically 100 nm line width, 10 nm height and 2-5 micron spacing) block diffusive transport of lipids, bilayer-associated protein ligands and their cognate receptors on the plasma membrane between isolated corrals, but they do not impose any effect on lateral diffusion within each corral[3, 23, 24, 29, 30]. Thus, when T cells interact with a protein-functionalized supported lipid bilayer on a nanopatterned substrate, TCR–pMHC microclusters and LFA-1–ICAM-1 assemblies form properly but cannot move outside the corral boundaries. Discontinuous barriers (crosses) that permit lateral diffusion of lipids and bilayer proteins serve as a control for nonspecific interactions of the cell with the metal barrier material. This system reliably reproduces the classic Kupferian synapse in T cells (**Figure 1B–G**).

Analysis of cortical actin flow in primary T cells

One effective way of imaging the movement of the actin cytoskeleton is fluorescence speckle microscopy (FSM)[31]. In this methodology, fluorescent probes are incorporated sparsely into the actin cytoskeleton, and intrinsic density fluctuations in their random distribution provide features, or 'speckles', whose movement can be tracked. FSM generally does not involve actual imaging of individual fluorophores, though this is possible with modern methods. Stochastic density fluctuations are readily discernable for up to ten fluorophores per diffraction spot. As such, coordinated translational movement of feature patterns mirrors bulk cytoskeletal flow, whereas time evolution of the translating pattern reflects dynamic redistribution of the monomers.

In the experiments described here, we performed FSM using relatively high fluorescent probe densities. This enables better mapping of actual actin density fluctuations (as opposed to stochastic labeling fluctuations) but also requires more sophisticated image analysis. At very low probe densities, speckle features tend to have simpler shapes than they do at higher density. Thus, simple particle tracking algorithms are easily foiled by the complex patterns seen in highly labeled cells. To improve tracking accuracy in these systems, we developed a set of algorithms (see **Materials and Methods**) that identify features in images based on shape-independent gradient tracking, link them across multiple frames and evaluate their motion. The vector-field algorithm that we employed is a modification of those commonly used in medical imaging applications[32], which isolate endpoints in the fluorescence intensity gradient of an image (**Figure 2A–C**). This method overcomes the tendency of raster-based algorithms to identify multiple false centers in features based on their multiple local fluorescence intensity maxima. Features are then tracked across consecutive frames using a modified nearest-neighbor approach (**Figure 2B and C**).

The most common parameter used for evaluating moving objects is velocity. Although this parameter has been used effectively to describe speckle motion, we found that imaging of the cytoskeleton through an opaque chromium pattern displaced the identified centers of actin features near pattern boundaries and impacted both their apparent speed and direction of travel. We therefore evaluated actin motion in terms of the time it took a feature to travel a certain distance, here referred to as the 'escape time' (t) and the 'escape distance' (r) (**Figure 2D**). This analysis method, explained in detail in the **Materials and Methods** section, is effectively a determination of mean square displacement, except that the output is in the form of time per (unit distance)^2 instead of the inverse. The escape time analysis is not biased by the direction of motion and demonstrably avoids the optical artifacts mentioned above. To test the effects of imaging artifacts, image stacks from cells on unpatterned substrates were overlaid with grid shadow images prior to analysis to simulate the appearance of cells on actual patterned substrates. The escape times in these cells showed no dependence on proximity to pattern boundaries. Escape times were also similar between cells expressing EGFP–UtrCH and EGFP–b-actin.

The primary purpose of the grid experiments was to pin the position of TCR microclusters so that changes in actin movement and fluctuations at these microclusters could be analyzed. Such analysis required binning the escape times of features based on spatial distribution (e.g. **Figure 2E**). Escape times were also normalized within each cell to facilitate comparison between different cells in a population, even in the presence of cell-to-cell variability. This normalization allowed statistically robust quantitative data sets to be assembled.

Resistance-dependent slowing of actin at sites of TCR clusters

In the following studies, T cells were allowed to form immunological synapses on substrates nanopatterned with metal grids. Grid barriers effectively trap TCR microclusters, pinning them in place for extended periods of time without otherwise interfering with their assembly. In cells that formed synapses on the edge of a patterned region, large bands of clustered TCR were visible at the pattern boundary. In these partially patterned cells, it was possible to compare escape times of features in regions with and without clustered TCRs that were approximately equidistant from the cell center (**Figure 3A**). As anticipated, escape times in a region corresponding to clustered TCRs were higher than those in a region lacking TCRs (**Figure 3B**). This can be interpreted as the result of slowing down or of concentration of actin in the immediate vicinity of the TCR cluster.

TCR visualization in cells fully on grid patterns is hindered by the overall small size of the structures. Nonetheless, based on the above observations as well as past reports, it is reasonable to assume that TCRs will be generally concentrated along the grid boundaries. With this information, the grids themselves become fiduciary markers of where TCR microclusters are enriched, and statistical analysis of the data can be performed without

the need for direct TCR imaging. For this analysis, all observable features in several cells were tracked, and measured escape times from each position in the cell were binned according to their proximity to zero, one vertical, one horizontal or two grid lines (**Figure 3C– H**). The results indicate that escape times increased near one gridline and greatly increased near two lines (corresponding to a grid corner) (**Figure 3C and F**). Because actin within the T cell can only interact with the metal substrate barriers through TCR–pMHC or possibly also LFA–ICAM interactions[8,18], the slowing of actin movement near grids reflects interactions between actin and these proteins on the cytoplasmic side of the T cell membrane. The escape times of all four populations remained essentially constant when cells interacted with control substrates of chromium crosses that did not block long-range TCR transport (**Figure 3D and G**) and when cells were not on grids (**Figure 3E and H**).

To determine whether actin features are slowed by the mere presence of TCRs or by resistance against their motion from barriers, the directional components of escape times parallel or perpendicular to grid lines were evaluated. These components referred to the amount of time it took a feature to traverse a total vector distance equivalent to the original escape distance in the x or y direction, as defined by the layout of the grid (**Figure 4**). The components of the escape time perpendicular to a barrier increased in the populations of features near that barrier, whereas components of the escape time parallel to the barrier were essentially unaffected (**Figure 4A–C**). Also unaffected by this analysis method were all components in cells interacting with diffusion-permissive substrates patterned with chromium crosses and all components in cells that were not on grids (**Figure 4D–I**). These data suggest that active resistance to TCR cluster motion (as opposed to the mere presence of TCRs) is necessary to induce a slowing of the cortical actin cytoskeleton and it is unlikely that the effect is an artifact of nonspecific cell interactions with chromium.

Coordinated actin fluctuations near TCRs

In time-lapse recordings of EGFP–b-actin, actin accumulations frequently appeared adjacent to substrate barriers. These accumulations transiently increased in intensity before dissipating to the background level of fluorescence without translocating past the barrier towards the center of the immunological synapse. Such large-scale fluctuations in total actin density indicate a large degree of coordination in the coupling between actin and T cell surface proteins, including TCRs. Although interactions between actin and TCRs have generally been described as dynamic, the nearly complete dissipation of actin accumulations observed here is somewhat unexpected. At the label densities used in these experiments, the observed fluctuations reflect real dissipation of the actin itself, rather than stochastic fluctuations in fluorophore density. We observed fluorescence intensity accumulations that were two to four times higher than the cell background level that exhibited near 100% variance (complete dissipation). This variance is more than an order of magnitude beyond what can be expected from stochastic fluctuations[33].

To better characterize the spatiotemporal dynamics of EGFP–b-actin, we developed a numerical approach based on time-autocorrelation of fluorescence intensity as a function of spatial position. This method is distinct from previously developed image correlation spectroscopy (ICS)[34] and spatiotemporal ICS (STICS)[35–37,37] in that there is no correlation of the spatial coordinates. Methods like ICS and STICS can be powerful ways to analyze the dynamics of protein clusters in cells, but they are limited in cases where the cluster sizes are heterogeneous. Our approach effectively identifies transient accumulations of arbitrary size with dynamics that are distinct from stochastic fluctuations in the EGFP–b-actin matrix.

In a typical EGFP–b-actin-labeled cell (**Figure 5A–C**), the EGFP–b-actin time-average is a weak indication of where and for how long accumulations occur (**Figure 5D**). However, the frame-by-frame fluorescence intensity profiles of areas corresponding to accumulations (**Figure 5D and E,** *blue areas and traces*) show discrete large-scale intensity fluctuations, whereas in nearby areas lacking accumulations (**Figure 5D and E,** *red areas and traces*) the fluorescence fluctuates on a much smaller scale around a background value. The time-autocorrelation functions of fluorescence intensity from the respective regions clearly reflect these differences (**Figure 5F**). This analysis can be readily applied to the entire image area, as shown in **Figure 5G**, where the integral of the autocorrelation function of each image pixel is plotted at the original pixel position. High autocorrelations in areas on the periphery of the cell correspond to extensions and retractions of the lamellipodia (**Figure 5G**, *white asterisks*), whereas locally high autocorrelations are visible at areas adjacent to substrate barriers (**Figure 5G,** *white arrows and others*). These latter areas correspond well to cytoskeletal accumulations visible in data recordings and to areas that contain a high TCR density prior to time-lapse recording (**Figure 5C**).

The involvement of actin in T cell signaling is well established, but recent studies have shown that beyond acting as a simple transport mechanism, the actin cytoskeleton actively modulates TCR recognition of antigen by altering TCR–pMHC kinetics[16,17]. To better understand how this modulation occurs, there is a need to move beyond bulk inhibition of the cytoskeleton with latrunculin, cytochalasin and similar compounds by probing specific receptor–actin interactions and using quantitative analysis methods to describe the outcomes. We used the hybrid live cell–nanopatterned supported lipid bilayer system to pin TCR clusters and developed specialized tracking algorithms and an image time-autocorrelation analysis to characterize properties of a mobile and fluctuating cytoskeletal network interacting with these receptor assemblies. Using these tools, we have shown that in primary T cells, actin slows down and assembles and disassembles *en masse* in the vicinity of TCR clusters.

The slowing and, to some extent, the overall average increase in density of actin at the sites of pinned TCR clusters are to be expected from a receptor–actin interaction that has previously been shown to be highly dissipative, or frictional[8,12,18]. However, such a coupling does not on its own give rise to the large transient actin enrichments, or

fluctuations, that we observe at these sites. We make this argument based on the fact that fluctuations in a random distribution of *n* independent objects scale with $\sqrt{n}$ [33]. Larger-scale fluctuations are indicative of coordination within the system. Here, proximity to TCR microclusters leads to increases in large cytoskeletal fluctuations, suggesting greater degrees of coordination within the actin network. Taken in the context of studies that have shown microclusters to survive actin disruption[14,15], this finding demonstrates that TCR microclusters are the more stable element in the TCR–actin interaction and that they template the dynamic actin around themselves.

Materials and Methods

DNA constructs

A plasmid containing EGFP fused to the calponin homology domain of utrophin (EGFP–UtrCH) was a gift of William Bement, University of Wisconsin, Madison, WI[28]. The EGFP–UtrCH gene was amplified using PCR and subcloned into a murine stem cell virus parent-vector-containing puromycin N-acetyltransferase expressed from an internal ribosome entry site (pMSCV-Puro) as previously described[38]. A retroviral-vector-containing EGFP–b-actin was similarly produced by subcloning the gene from an EGFP–b-actin-containing pCDNA3 vector[39].

Retroviral transduction of T cells

AND CD4+ T cells[40] were harvested and retrovirally transduced as previously described[38]. Briefly, retrovirus-containing cell medium was harvested from cultures of Phoenix retroviral packaging cells transfected with pMSCV-Puro containing the gene of interest. The medium was used to transduce CD4+ T cells isolated from the lymph nodes and spleens of AND 6 B10.BR mice, primed with 2μM moth cytochrome c (amino acids 88–103) and stimulated with 50 U/ml of interleukin-2 (IL-2). T cells were transduced 48 and/or 72 hours after isolation, selected using 0.5 μg/ml puromycin from 78 to 120 hours after isolation and used in experiments 168 hours after isolation.

Preparation of T cells for imaging

Imaging experiments were performed as previously described (Smith et al., 2011). Briefly, supported lipid bilayers containing 2 mol% Ni^{2+}-DOGS and 98 mol% DOPC (Avanti Polar Lipids, Alabaster, AL) were formed within FCS2 Closed Chamber Systems (flow cells; Bioptechs, Butler, PA) on piranha-etched glass cover slips or patterned chromium substrates nanofabricated using electron beam lithography as previously described[30]. The bilayers were functionalized with polyhistidine-tagged MHC loaded with moth cytochrome c (amino acids 88–103) and with polyhistidine-tagged ICAM-1 proteins, and the flow cells were brought to 37°C. T cells were rinsed with a previously described imaging buffer[38],

pelleted, re-suspended in a solution of 5 ml Alexa-Fluor-568- or -647-labeled H57 anti-TCR antibody fragment (Fab) diluted in 100 µl imaging buffer and incubated on ice for 20 minutes. Cells were then rinsed with imaging buffer, pelleted, re-suspended in pre-warmed imaging buffer and injected into flow cells. The flow cells were kept at 37°C throughout the experiments and all images were acquired within 120 minutes of the injection of the cells.

Microscopy

Cell imaging was performed on an inverted microscope (Nikon Eclipse Ti; Technical Instruments, Burlingame, CA). TIRF microscopy was done using a fiber-coupled Nikon TIRF illuminator with a custom-built laser source[38]. The 647 nm (RCL-050-640; Crystalaser, Reno, NV), 561 nm (GCL-100-561; Crystalaser, Reno, NV) and 488 nm (Sapphire HP; Coherent, Santa Clara, CA) lasers were launched into a single-mode fiber that was connected to the TIRF illuminator. Excitation powers at the sample were on the order of 1 kW/cm^2. Images were acquired with an Orca-R2 digital camera (C10600-10B; Hamamatsu Photonics K.K., Japan).

Actin motion analysis

To analyze the motion of the actin cytoskeleton, we developed a set of algorithms for identifying and tracking visibly mobile fluctuations in actin and/or probe density and implemented them in MatLab. Features in the actin distribution are first identified using a supplemented image gradient approach. Each frame of an actin time-lapse recording is convolved with a Gaussian filter to remove low-level imaging noise, and local maxima in the fluorescence intensity image are used to identify candidate features. Because individual features often contain multiple fluorescence intensity maxima, vector fields are created based on fluorescence intensity gradients within the image, and features are assigned locations by positions with converging vectors, which correspond to low local intensity variations. The vector fields also overcome uneven levels of fluorescence across the cell, thus allowing features to be identified consistently in spite of subcellular variations in cytoskeletal density or illumination[32]. Following identification, nearest neighbor features in consecutive frames are linked to generate actin trajectories as previously described[18]. Briefly, linking is performed only on features that are visible in consecutive frames within 5 pixels (0.315 µm) of each other. The appearances and disappearances of features are monitored such that if a feature is present in frame t and has no identifiable nearest neighbor in frame *t+1*, it is defined as disappearing after frame *t*. Mergers and splits of features are also monitored. The trajectories of actin features are evaluated using an algorithm that determines the time it takes each feature to move a certain distance. We refer to this time as the 'escape time' (*t*) to signify that there is no directional bias to the algorithm, and the selected 'escape distance' (r=3 pixels=0.189 µm) thus defines a circular boundary around the feature. Note that although the escape distance is below the Rayleigh diffraction limit, it is still possible to localize maxima in the light field with high precision. Our approach is based on centroid analyses used in single molecule localization

algorithms[41, 42] except that we are tracking inhomogeneities in the fluorophore density field rather than single objects. This is fundamentally analogous to single fluorophore position identification in standard super-resolution optical techniques such as photoactivated localization microscopy[43] and stochastic optical reconstruction microscopy[44]. Escape times are determined iteratively for each frame in which a given feature is identified. They are not recorded when a feature disappears before exceeding the escape distance.

Image time-autocorrelation analysis

The time-autocorrelation function of the fluctuating fluorescence intensity was calculated on a pixel-by-pixel basis using the time-lapse image stacks. The time-dependent intensity of each pixel is designated at $I_{x,y}(t)$, where the x and y subscripts refer to the pixel position. The correlation function was calculated using the fluctuations of the intensity away from the time-averaged value:

$$\partial I_{x,y}(t) = I_{x,y}(t) - \langle I_{x,y}(t) \rangle \text{ (where } \langle I_{x,y}(t) \rangle = \frac{1}{T}\int_0^T I_{x,y}(t)dt \text{.)}$$

The pixel-by-pixel time-autocorrelation function is then calculated as

$$G_{x,y}(\tau) = \frac{\langle \partial I_{x,y}(t) \cdot \partial I_{x,y}(t+\tau) \rangle}{\langle I_{x,y}(t) \rangle^2}$$

Chapter 3 References

1. Grakoui, A. *et al.* The immunological synapse: a molecular machine controlling T cell activation. *Science* **285,** 221–227 (1999).

2. Monks, C. R., Freiberg, B. A., Kupfer, H., Sciaky, N. & Kupfer, A. Three-dimensional segregation of supramolecular activation clusters in T cells. *Nature* **395,** 82–86 (1998).

3. Mossman, K. D., Campi, G., Groves, J. T. & Dustin, M. L. Altered TCR Signaling from Geometrically Repatterned Immunological Synapses. *Science* **310,** 1191–1193 (2005).

4. Lee, K.-H. *et al.* T cell receptor signaling precedes immunological synapse formation. *Science* **295,** 1539–1542 (2002).

5. Yokosuka, T. *et al.* Newly generated T cell receptor microclusters initiate and sustain T cell activation by recruitment of Zap70 and SLP-76. *Nat. Immunol.* **6,** 1253–1262 (2005).

6. Dustin, M. L., Chakraborty, A. K. & Shaw, A. S. Understanding the structure and function of the immunological synapse. *Cold Spring Harb. Perspect. Biol.* **2,** a002311 (2010).

7. Barda-Saad, M. *et al.* Dynamic molecular interactions linking the T cell antigen receptor to the actin cytoskeleton. *Nat. Immunol.* **6,** 80–89 (2005).

8. DeMond, A. L., Mossman, K. D., Starr, T., Dustin, M. L. & Groves, J. T. T cell receptor microcluster transport through molecular mazes reveals mechanism of translocation. *Biophys. J.* **94,** 3286–3292 (2008).

9. Gomez, T. S. & Billadeau, D. D. T cell activation and the cytoskeleton: you can't have one without the other. *Adv. Immunol.* **97,** 1–64 (2008).

10. Ryser, J. E., Rungger-Brändle, E., Chaponnier, C., Gabbiani, G. & Vassalli, P. The area of attachment of cytotoxic T lymphocytes to their target cells shows high motility and polarization of actin, but not myosin. *J. Immunol. Baltim. Md 1950* **128,** 1159–1162 (1982).

11. Bunnell, S. C., Kapoor, V., Trible, R. P., Zhang, W. & Samelson, L. E. Dynamic actin polymerization drives T cell receptor-induced spreading: a role for the signal transduction adaptor LAT. *Immunity* **14,** 315–329 (2001).

12. Kaizuka, Y., Douglass, A. D., Varma, R., Dustin, M. L. & Vale, R. D. Mechanisms for segregating T cell receptor and adhesion molecules during immunological synapse formation in Jurkat T cells. *Proc. Natl. Acad. Sci. U. S. A.* **104,** 20296–20301 (2007).

13. Burkhardt, J. K., Carrizosa, E. & Shaffer, M. H. The actin cytoskeleton in T cell activation. *Annu. Rev. Immunol.* **26,** 233–259 (2008).

14. Campi, G., Varma, R. & Dustin, M. L. Actin and agonist MHC-peptide complex-dependent T cell receptor microclusters as scaffolds for signaling. *J. Exp. Med.* **202,** 1031–1036 (2005).

15. Varma, R., Campi, G., Yokosuka, T., Saito, T. & Dustin, M. L. T cell receptor-proximal signals are sustained in peripheral microclusters and terminated in the central supramolecular activation cluster. *Immunity* **25,** 117–127 (2006).

16. Huppa, J. B. *et al.* TCR–peptide–MHC interactions in situ show accelerated kinetics and increased affinity. *Nature* **463,** 963–967 (2010).

17. Huang, J. *et al.* The kinetics of two-dimensional TCR and pMHC interactions determine T-cell responsiveness. *Nature* **464,** 932–936 (2010).

18. Yu, C., Wu, H.-J., Kaizuka, Y., Vale, R. D. & Groves, J. T. Altered Actin Centripetal Retrograde Flow in Physically Restricted Immunological Synapses. *PLoS ONE* **5,** e11878 (2010).

19. Hartman, N. C., Nye, J. A. & Groves, J. T. Cluster size regulates protein sorting in the immunological synapse. *Proc. Natl. Acad. Sci.* **106,** 12729–12734 (2009).

20. Tanimura, N. *et al.* Dynamic changes in the mobility of LAT in aggregated lipid rafts upon T cell activation. *J. Cell Biol.* **160,** 125–135 (2003).

21. Bartelt, R. R., Cruz-Orcutt, N., Collins, M. & Houtman, J. C. D. Comparison of T Cell Receptor-Induced Proximal Signaling and Downstream Functions in Immortalized and Primary T Cells. *PLoS ONE* **4,** e5430 (2009).

22. Dobson-Belaire, W. N., Cochrane, A., Ostrowski, M. A. & Gray-Owen, S. D. Differential response of primary and immortalized CD4+ T cells to Neisseria gonorrhoeae-induced cytokines determines the effect on HIV-1 replication. *PloS One* **6,** e18133 (2011).

23. Groves, J. T., Ulman, N. & Boxer, S. G. Micropatterning Fluid Lipid Bilayers on Solid Supports. *Science* **275,** 651–653 (1997).

24. Manz, B. N. & Groves, J. T. Spatial organization and signal transduction at intercellular junctions. *Nat. Rev. Mol. Cell Biol.***11,** 342–352 (2010).

25. Mossman, K. & Groves, J. Micropatterned supported membranes as tools for quantitative studies of the immunological synapse. *Chem. Soc. Rev.* **36,** 46–54 (2007).

26. Nye, J. A. & Groves, J. T. Kinetic control of histidine-tagged protein surface density on supported lipid bilayers. *Langmuir ACS J. Surf. Colloids* **24,** 4145–4149 (2008).

27. Dustin, M. L. Supported bilayers at the vanguard of immune cell activation studies. *J. Struct. Biol.* **168,** 152–160 (2009).

28.Burkel, B. M., von Dassow, G. & Bement, W. M. Versatile fluorescent probes for actin filaments based on the actin-binding domain of utrophin. *Cell Motil. Cytoskeleton* **64,** 822–832 (2007).

29. Groves, J. T. & Boxer, S. G. Micropattern formation in supported lipid membranes. *Acc. Chem. Res.* **35,** 149–157 (2002).

30. Salaita, K. *et al.* Restriction of Receptor Movement Alters Cellular Response: Physical Force Sensing by EphA2. *Science* **327,** 1380–1385 (2010).

31. Waterman-Storer, C. M., Desai, A., Bulinski, J. C. & Salmon, E. D. Fluorescent speckle microscopy, a method to visualize the dynamics of protein assemblies in living cells. *Curr. Biol. CB* **8,** 1227–1230 (1998).

32. Xu, C. & Prince, J. L. Snakes, shapes, and gradient vector flow. *IEEE Trans. Image Process. Publ. IEEE Signal Process. Soc.* **7,** 359–369 (1998).

33. McQuarrie, D. *Statistical Mechanics*. (University Science Books, 2000).

34. Petersen, N. O., Höddelius, P. L., Wiseman, P. W., Seger, O. & Magnusson, K. E. Quantitation of membrane receptor distributions by image correlation spectroscopy: concept and application. *Biophys. J.* **65,** 1135–1146 (1993).

35. Rossow, M., Mantulin, W. W. & Gratton, E. Spatio-Temporal Image Correlation Spectroscopy Measurements of Flow Demonstrated in Microfluidic Channels. *J. Biomed. Opt.* **14,** 024014 (2009).

36. Kulkarni, R. P., Wu, D. D., Davis, M. E. & Fraser, S. E. Quantitating intracellular transport of polyplexes by spatio-temporal image correlation spectroscopy. *Proc. Natl. Acad. Sci. U. S. A.* **102,** 7523–7528 (2005).

37. Wiseman, P. W. *et al.* Spatial mapping of integrin interactions and dynamics during cell migration by image correlation microscopy. *J. Cell Sci.* **117,** 5521–5534 (2004).

38. Smith, A. W., Smoligovets, A. A. & Groves, J. T. Patterned Two-Photon Photoactivation Illuminates Spatial Reorganization in Live Cells. *J. Phys. Chem. A* **115,** 3867–3875 (2011).

39. Ballestrem, C., Wehrle-Haller, B. & Imhof, B. A. Actin dynamics in living mammalian cells. *J. Cell Sci.* **111,** 1649–1658 (1998).

40. Kaye, J. *et al.* Selective development of CD4+ T cells in transgenic mice expressing a class II MHC-restricted antigen receptor. *Nature* **341,** 746–749 (1989).

41. Thompson, R. E., Larson, D. R. & Webb, W. W. Precise Nanometer Localization Analysis for Individual Fluorescent Probes. *Biophys. J.* **82,** 2775–2783 (2002).

42. Saxton, M. J. in *Fundam. Concepts Biophys.* (Jue, T.) 1–33 (Humana Press, 2009). at <http://link.springer.com/chapter/10.1007/978-1-59745-397-4_6>

43. Betzig, E. *et al.* Imaging Intracellular Fluorescent Proteins at Nanometer Resolution. *Science* **313,** 1642–1645 (2006).

44. Rust, M. J., Bates, M. & Zhuang, X. Sub-diffraction-limit imaging by stochastic optical reconstruction microscopy (STORM). *Nat. Methods* **3,** 793–796 (2006).

Chapter 3 Figures

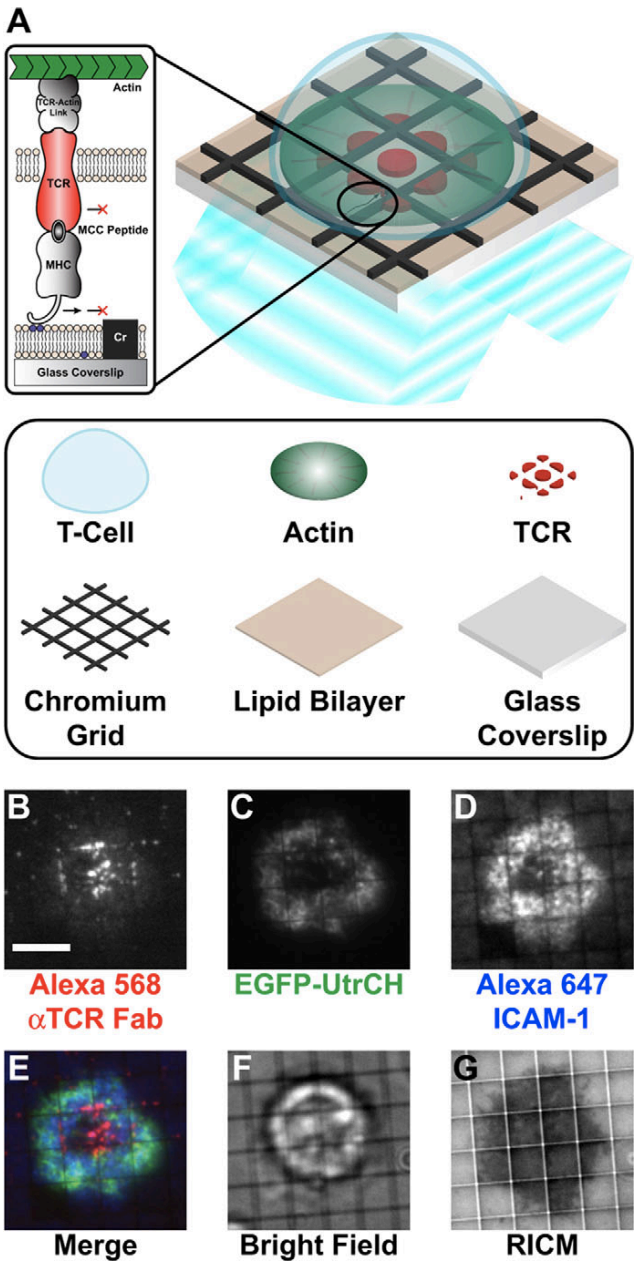

Figure 1. *The supported lipid bilayer allows visualization of the T cell cortical actin cytoskeleton during immunological synapse formation.*

(A) Schematic outline of the experiment. T cells interact with a supported lipid bilayer functionalized with APC proteins. Centripetal flow of the actin cytoskeleton causes TCR microclusters to coalesce and translocate until they reach a chromium barrier (Cr), where they accumulate. The ICAM-1 APC protein (not shown) is also included and interacts with T cell LFA-1. Ni^{2+}-DOGS lipids (purple circles) and the TIRF illumination beam (cyan) are not labeled. **(B–G)** TIRF microscopy images of TCRs, the actin cytoskeleton and ICAM-1, as well as bright field and reflection interference contrast microscopy (RICM) images of a cell on a grid-patterned substrate show a typical frustrated immunological synapse. Scale bar: 5μm.

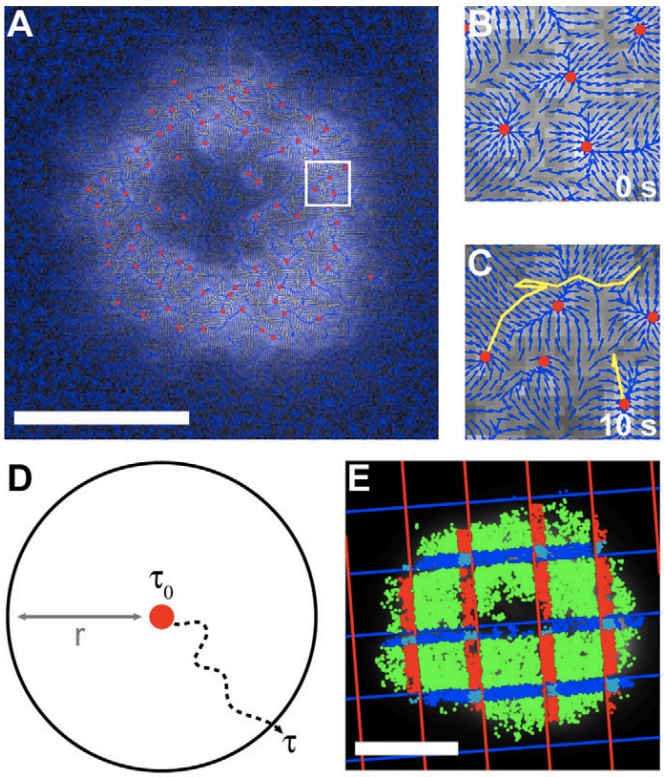

Figure 2. *Analysis methods for bulk cytoskeletal flow are distinct from those used to describe speckle motion.* **(A)** A vector-field algorithm identifies the centers of actin features across a whole cell. **(B,C)** The white square in A is enlarged to clearly show individual vectors in the vector field, and actin features are tracked across multiple frames. New features without tracks are also visible in **C**. **(D)** Schematic of the escape time analysis. The time it takes for a feature to travel further than a given escape distance (r) in any direction is its escape time (t). **(E)** Escape times are distributed into populations based on each feature's instantaneous position. For example, features within 0.63 μm (10 pixels) of a single pattern boundary and on the opposite side from the cell center are colored dark blue or red, those within 0.63 μm of two boundaries are colored light blue and all other features are colored green. Scale bars: 5 μm.

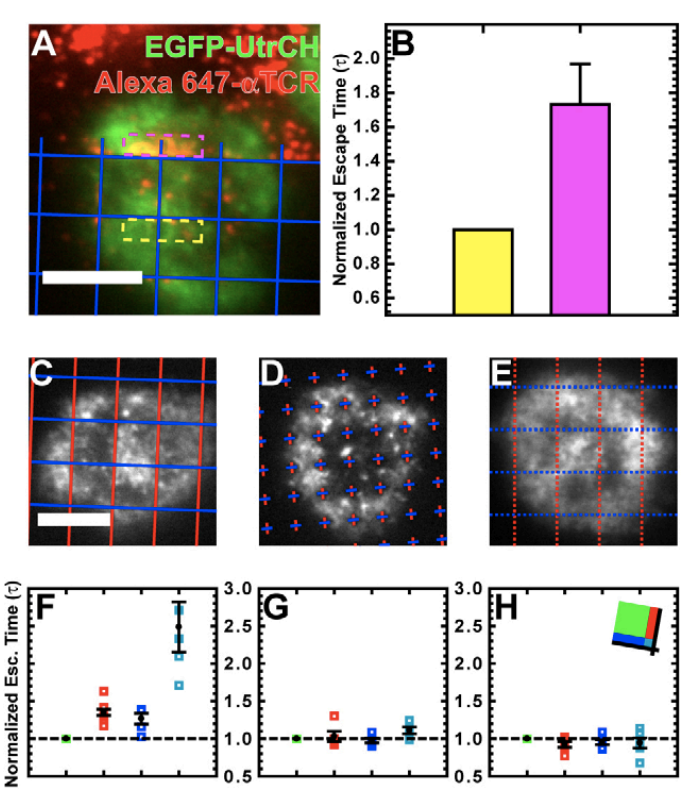

Figure 3. *Actin features slow down in TCR-rich regions.* **(A, B)** Two regions of a cell partially on a grid-patterned supported lipid bilayer equidistant from the cell center were selected (yellow and purple rectangles in **A**) for analysis of actin escape times **(B). (C–E)** Representative frames from time lapses show cells interacting with a grid-patterned substrate **(C),** a cross-patterned substrate **(D)** or an unpatterned substrate overlaid with the grid used for analysis **(E)**. **(F–H)** Actin features from the cells in **C–E** were partitioned into four populations and analyzed for escape times. The inset shows that the green population is composed of all steps occurring further than 0.63 μm (10 pixels) from the outside edge of a grid line, the dark blue and red populations are composed of steps occurring within 0.63 μm of an x or y gridline, respectively, and the light blue population is composed of steps occurring within 0.63 μm of both grid lines. Error bars represent s.e.m. Scale bars: 5 μm.

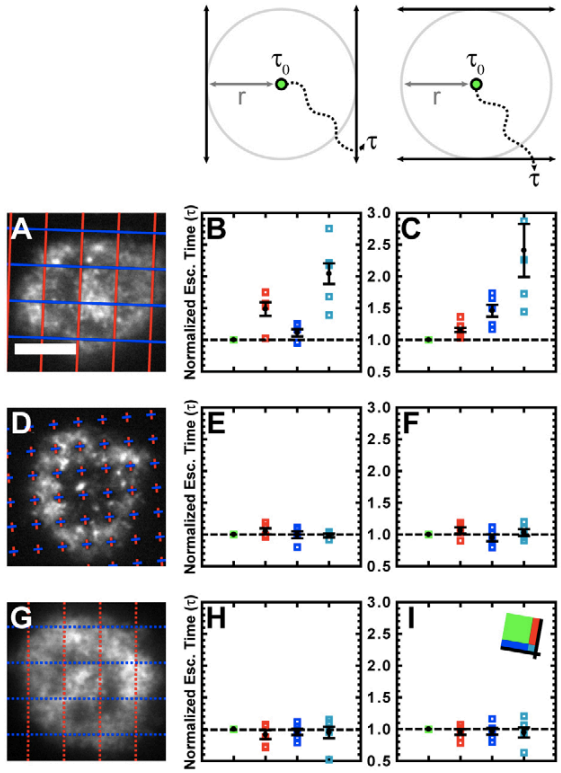

Figure 4. *Increased actin escape times correspond to motion perpendicular to TCR diffusion barriers.* **(A,D,G)** Representative frames from time lapses show cells interacting with a grid-patterned substrate **(A)**, a cross-patterned substrate **(D)** or an unpatterned substrate overlaid with the grid used for analysis **(G)**. **(B,E,H)** The escape time analysis from Fig. 3 was repeated for the cells in **A, D, G,** but the escape time was redefined as the time it takes for a feature to move outside of an area identified by boundaries tangential to the original escape area and parallel to the y grid line (*schematic above column*). This in effect considers only the x component of motion of the feature. **(C,F,I)** The escape time analysis from Fig. 3 was repeated for the cells in **A,D,G**, but the escape time was redefined as the time it takes for a heterogeneity to move outside of an area identified by boundaries tangential to the original escape area and parallel to the x grid line (schematic above column). This in effect considers only the y component of motion of the feature. Error bars represent standard error of the mean. Scale bars: 5μm.

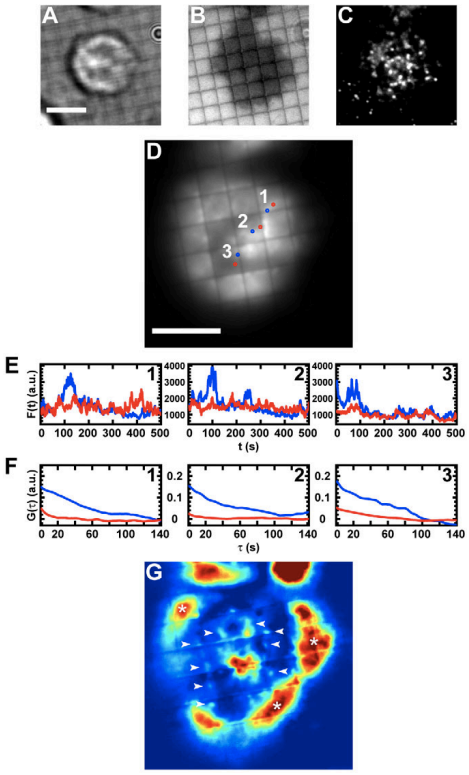

Figure 5. *Transient enrichments of the actin cytoskeleton occur at TCR clusters.* **(A–C)** Images taken before cytoskeletal time-lapse recording show the bright field **(A)**, RICM **(B)** and TCR channel **(C)** views of an EGFP–b actin-labeled cell. **(D)** The entire cytoskeletal time-lapse recording was time-averaged and areas corresponding to actin accumulations (blue regions 1, 2 and 3) and nearby background areas (red regions 1, 2 and 3) selected. **(E)** Fluorescence intensity profile over time is shown for each pixel within the regions selected in D. **(F)** Autocorrelation of the results shown in E. **(G)** The integral of the autocorrelation of the fluorescence intensity profile of every pixel in the cytoskeletal time-lapse image stack is output in the x–y location corresponding to its original pixel and displayed according to a color scale of arbitrary units. The white asterisks correspond to areas of extension and retraction of the lamellipodia and the white arrows highlight areas of high autocorrelation due to putative actin accumulations. Scale bars: 5 μm.